Binder Jet Printing of a Low-Cost Tool Steel Powder

by

Ryan Ley

Submitted in partial fulfilment of the requirements
for the degree of Master of Applied Science

at

Dalhousie University
Halifax, Nova Scotia
November 2022

Table of Contents

List of Tables iv

List of Figures v

Abstract viii

List of Abbreviations Used ix

Acknowledgements x

CHAPTER 1 – INTRODUCTION 1

1.1 Tool Steel Metallurgy 1

1.1.1 Categories/Alloys 1

1.1.2 Heat Treatments 5

1.1.3 Microstructures 5

1.1.4 Mechanical Properties 7

1.2 Binder Jet Printing Technology 8

1.2.1 Powder Feedstock Production 9

1.2.2 Binder Systems 10

1.2.3 Printing Concept 12

1.2.4 Curing and Debinding 13

1.2.5 Sintering 13

1.2.6 Post-Sintering Operations 17

1.3 Commercial Binder Jet Materials 19

1.4 Applications for Binder Jet Printing 20

CHAPTER 2 – RESEARCH OBJECTIVES 24

CHAPTER 3 – BINDER JET PRINTING OF A LOW-COST TOOL STEEL POWDER 25

Abstract 25
3.1 Introduction 26
3.2 Materials 28
3.3 Experimental Techniques 30
3.4 Results 32
3.4.1 Sintering Response 32
3.4.2 Comparison to Wrought D2 48
3.5 Conclusions 56
3.6 Acknowledgements 57
CHAPTER 4 – SUMMARY AND CONCLUSIONS 58
4.1 Future Work 60
References 61

List of Tables

Table 1 - Nominal alloying addition ranges for different types of tool steels [1]..... 3

Table 2 - A simplified overview of the mechanical properties of various types of tool steels [2] 8

Table 3 – Composition of the WA D2 powder utilized (all values in weight %) as compared to the chemical specifications for wrought D2 [1]. 28

Table 4 - Densities of samples sintered in the thermal dilatometer at various temperatures. 38

Table 5 - The measured hardness values for as-sintered, as-received, and heat-treated binder jet printed and wrought D2 samples. 55

Table 6 – Summary of compressive properties measured for wrought and BJP materials in a heat treated state. 56

List of Figures

Figure 1 - An SEM image depicting the microstructure of partially remelted D2 tool steel [7]. 7

Figure 2 - A schematic showing key stages of BJP including printing, curing, de-powdering, and sintering [9]. 9

Figure 3 - SEM images showing the morphological differences between (a) gas-atomized and (b) water-atomized stainless steel powder [13]. 10

Figure 4 – A comparison between (a) thermoset polymer and (b) nanoparticle containing binders for BJP [9, 15]. 11

Figure 5 – A schematic of the binder jet printing process [14]. 12

Figure 6 – The possible processes for achieving full or near-full density in a BJP part [9]. 14

Figure 7 - A depiction of liquid phase sintering [22]. 16

Figure 8 – Size comparison between an as-printed and sintered sample of Ni-based superalloy 625 [26]. 18

Figure 9 – BJP titanium carbide parts with complex geometries, (a) helical gear and (b) "spider web" lattice truss [30]. 21

Figure 10 – Several examples of metal parts produced via BJP. (a) An extrusion die used in plastic extrusion, shown here composed of H13 tool steel [43]. (b) A thermostat housing replacement for a vintage Mercedes Benz engine, shown here composed of 316L stainless steel [44]. (c) A custom-made putter head for golf clubs, shown here made from 17-4 PH stainless steel [45]. 23

Figure 11 - Particle size distribution measured for the WA D2 powder. 29

Figure 12 – Morphology of the WA D2 powder. 29

Figure 13 – Pseudo-phase diagram generated in FactSage for the measured D2 composition with varying carbon content. 33

Figure 14 – Thermodynamic data for the D2 system illustrating (a) various phase transitions predicted to occur on heating from 500°C to 1500°C and (b) a more detailed view of the liquid phase evolution. 34

Figure 15 – DSC curves acquired from D2 powder samples heated to 1400°C. Data presented for (a) heating and (b) cooling. 36

Figure 16 – Thermodilatometry results for D2 specimens sintered between 1220°C and 1280°C. 37

Figure 17 - Comparison between dilatometry samples sintered at 1300°C (left) and in the de-bound condition (right). 38

Figure 18 – Micrographs of the dilatometer sintered samples at 200x magnification, sintered at (a) 1220°C, (b) 1240°C, (c) 1250°C, and (d) 1260°C for 30 minutes. 40

Figure 19 – Microstructures in dilatometer sintered samples sintered at (a) 1220°C, (b) 1240°C, (c) 1250°C, and (d) 1260°C as observed with a SEM. 41

Figure 20 – EDS mapping results for a dilatometer sample sintered at 1260°C showing (a) the original SEM image, as well as elemental maps for (b) vanadium, (c) chromium, (d) iron, and (e) carbon. 42

Figure 21 – Thermodilatometry curves for printed D2 specimen held at 1250°C for various periods. 43

Figure 22 – Micrographs of the dilatometer sintered samples at 200x magnification, sintered at 1250°C for (a) 10 minutes, (b) 30 minutes, (c) 60 minutes, and (d) 90 minutes. 44

Figure 23 - SEM images of the dilatometer sintered samples, held at 1250°C for (a) 10, (b) 30, (c) 60, and (d) 90 minutes. 45

Figure 24 – Comparison of sintered densities for binder jet printed dilatometry cylinders and TRS bars as a function of sintering temperature. All samples sintered at temperature for 30 minutes under a high vacuum atmosphere. 46

Figure 25 – Micrographs of TRS samples sintered at (a) 1220°C, (b) 1240°C, (c) 1250°C, and (d) 1260°C for 30 minutes under high vacuum. 47

Figure 26 - SEM images of the batch sintered TRS samples, sintered at (a) 1220°C, (b) 1240°C, (c) 1250°C, and (d) 1260°C for 30 minutes. 48

Figure 27 – DSC traces for wrought and BJP D2 samples in the annealed and as-sintered (1250°C for 30 minutes) conditions respectively. 50

Figure 28 - DSC traces acquired from wrought and BJP D2 samples after heat treatment. BJP sample sintered at 1250°C for 30 minutes. 51

Figure 29 – Microstructures of (a) BJP and (b) wrought D2 specimen after heat treatment. BJP sample originally sintered at 1250°C for 30 minutes. 52

Figure 30 – EDS mapping of a heat-treated BJP D2 sample, showing (a) the original SEM image, as well as the spatial distributions of (b) vanadium, (c) chromium, (d) iron, and (e) carbon. BJP sample originally sintered at 1250°C for 30 minutes. 53

Figure 31 – EDS mapping of a heat-treated wrought D2 sample, showing (a) the original SEM image, as well as the spatial distributions of (b) vanadium, (c) chromium, (d) iron, and (e) carbon. 54

Figure 32 – Compressive engineering stress-strain curves for heat treated D2 specimens processed through wrought forming and BJP. 56

Abstract

Water atomization is a commonly used process to inexpensively produce large volumes of powders for press-and-sinter powder metallurgy. While the resulting powder particles are typically irregularly shaped and relatively coarse, adjustments to the atomization parameters can yield particles that are finer in size and nominally spherical, thereby facilitating their potential for application in additive manufacturing (AM). Thus, the objective of this research was to investigate the viability of water atomized D2 tool steel powder in the context of binder jet printing (BJP). Builds were printed, cured, de-bound, and sintered under various conditions to assess densification behaviour. Optimal sintering conditions for maximum density (98.5% theoretical) without significant distortion or grain coarsening were determined to be 1250°C for 30 min under high vacuum. Printed samples underwent a standard heat treatment process for wrought D2 and performed comparably to the wrought counterpart in terms of hardness (6.6% difference) and compressive elastic modulus (0.5% difference) with offset yield stress showing the largest difference (12.2% difference). Heat-treated BJP samples retained key microstructural features imparted by the printing process such as carbide clusters within large grains and intergranular lamellae of eutectic carbides and prior austenite, whereas the wrought microstructure was largely homogenous with fine grains and carbides.

List of Abbreviations Used

AM	Additive manufacturing
BJP	Binder jet printing
DED	Directed energy deposition
DSC	Differential scanning calorimetry
EDS	Energy dispersive spectroscopy
ICP-OES	Inductively coupled plasma optical emission spectrometry
LPS	Liquid phase sintering
SEM	Scanning electron microscope
SLM	Selective laser melting
TRS	Transverse rupture strength
WA	Water atomized
wt.%	Weight percent

Acknowledgements

The author would like to thank the Natural Sciences and Engineering Research Council of Canada (NSERC) Holistic Innovation in Additive Manufacturing (HI-AM) Network for funding for this research and GKN Sinter Metals for providing the stock water atomized D2 powder used in this work.

I would like to personally thank Dr. Paul Bishop for taking me on as a graduate student and for his support and guidance which proved to be immensely valuable throughout this research. I would also like to thank the other members of my examining committee, Mr. Ian Donaldson and Dr. Andrew Corkum, for their support and insight.

Additional thanks to Mr. Randy Cooke and Dr. Addison Rayner for their technical assistance and training, as well as Mr. Albert Murphy and Mr. Mark MacDonald for machining samples and Ms. Patricia Scallion for training and guidance with microscopy. Finally, a special thank you to my fellow graduate students for their unending support, kindness, and assistance, and to my family for their love and support not only during the course of this research but also throughout my entire life.

CHAPTER 1 – INTRODUCTION

1.1 Tool Steel Metallurgy

Tool steels are a type of steel used primarily as tools in cutting, forming, or shaping processes [1]. They are similar to some alloy, carbon, or high-speed steels but have increased strength, toughness and wear resistance. These properties are integral to the many functions of tool steels, including tools, dies, and molds for cutting, forming, and shaping other metals or plastics [2]. As well, some tool steels have seen use as components in machinery or structures, such as springs or bearings for high temperature use [1].

Tool steels provide a multitude of services which typically subject them to high loads, often cyclic and at high temperatures, and must withstand many uses without breaking, wear, or deformation. These properties cannot be met by any individual tool steel, which is why there are a variety of tool steels with various mechanical and thermal properties, each split up into different categories depending on the primary alloying elements and application of the alloy [1].

Tool steels have been traditionally wrought materials, however powder metallurgy has also been used to achieve uniformity in carbide size and distribution, as well as being able to produce unique tool steel compositions which are difficult or impossible to replicate using other methods [1].

1.1.1 Categories/Alloys

The American Iron and Steel Institute (AISI) categorizes tool steels into 9 groups, each with their own letter designation: water-hardening (W), shock-resistant (S), oil-hardening (O), air-hardening (A), high-carbon and -chromium (D), mold steels (P), hot-work (H), tungsten high-speed (T), and molybdenum high-speed (M) [2]. This categorization takes into account several characteristics of the alloys such as alloying elements, applications, and heat-treatments. For example, types W, O, and A are defined by their method of post heat treatment quenching, whereas D, T, and M are defined by their respective major

alloying elements [2]. The typical composition ranges for each of these tool steels is presented in Table 1 below.

In terms of specific properties, the D types are particularly resistant to abrasion, and those which contain molybdenum are more likely to retain their shape during heat treatment [3]. Type H steels can be sub-categorized based on the prominent alloying elements. Types H10 to H19 have a set chromium content, and those containing molybdenum are particularly tough and are often cold worked for added hardness while retaining their toughness [3]. Types H21 to H26, however, are defined by a set tungsten content and are typically used in high temperature applications where their resistance to softening is necessary, but suffer from reduced toughness as a result [3].

Type W tool steels have low hardenability due to their low alloy content, and thus must be quenched to form surface martensite. As the alloying content is low, the sole carbides present within the martensite matrix are iron carbides. These tool steels do have a relatively high carbon content, which serves to provide exceptional hardness to the formed martensite [2].

Type S tool steels have a moderate carbon content which provides an increase in toughness due to fine carbides dispersed throughout the martensitic matrix. As these tool steels contain more alloying elements than the W types, type S tool steels have higher hardenability. Overall, these alloys have high strength and toughness and are resistant to wear and fracture during impacts [2].

Table 1 - Nominal alloying addition ranges for different types of tool steels [1].

Tool Steel	C	Mn	Si	Cr	Ni	Mo	W	V	Co
M type	0.75 - 1.52	0.15 - 0.60	0.15 - 0.65	3.50 - 4.75	<0.30	7.50 - 11.00 3.25 - 7.00	1.15 - 3.00 5.00 - 7.00 9.50 - 10.50	0.95 - 4.50	4.50 - 12.25
T type	0.65 - 0.90 1.50 - 1.60	0.10 - 0.40	0.15 - 0.40	3.75 - 5.00	<0.30	0.40 - 1.25 <1.00	17.25 - 21.00 11.75 - 14.75	0.80 - 5.25	7.00 - 13.00 4.25 - 5.75
H type	0.22 - 0.55	0.15 - 0.70	0.8 - 1.20 0.15 - 0.60	1.75-5.50 11.00-12.75	<0.30	1.10 - 3.00 0.30 - 0.55 -	<1.70 3.75 - 4.50 8.50 - 19.00	<1.20 1.75 - 2.20 0.25 - 1.25	- 4.00 - 4.50 -
A type	0.65 - 1.50 2.00 - 2.85	1.80 - 2.50 <1.00	<0.50	0.90-2.20 4.75-5.75	<0.30 1.25 - 2.05 <0.30	0.90 - 1.80	- - 0.50 - 1.50	- 0.15 - 1.40 3.90 - 5.15	-
D type	1.40 - 1.60 2.15 - 2.50	<0.60	<0.60	11.00-13.50	<0.30	0.70 - 1.20	<1.00	<1.00 3.80 - 4.40	<3.50 -
O type	0.85 - 1.55	0.3 - 1.80	<1.50	<0.85	<0.30	<0.30	0.40 - 2.00	<0.40	-
S type	0.40 - 0.65	0.10 - 1.50	0.15 - 2.50	<1.80 3.00-3.50	<0.30	<1.35 1.30 - 1.80	1.50 - 3.00 -	<0.5	-
L type	0.45 - 1.00	0.10 - 0.90	<0.50	0.60-1.20	<2.00	<0.50	-	0.10 - 0.30	-
P type	<0.40	0.10 - 1.00	<0.80	0.40-2.50	3.25 - 4.25 <1.50	- <1.00	-	-	-
W type	0.70 - 1.50	0.10 - 0.40	0.10 - 0.40	<0.60	<0.20	<0.10	<0.15	<0.35	-

Types O, A, and D tool steels share several similarities across their properties and processing methods. Type A tool steels can have a wide range of hardness and toughness as their alloy and carbon content can vary greatly across the different grades, but generally alloys within these three groupings typically have very high hardness and wear resistance at lower temperatures thanks to a microstructure consisting of high carbon martensite and alloy carbides. As a result of these properties, these types of tool steels are typically used as low-temperature machining tools. Due to their high carbon and alloying element content, these microstructures can be formed without the need for a water quench. Type A and D alloys can be air quenched, but due to its lower alloying element content, type O steels must be oil quenched to form the desired microstructure. As both oil and air quenching produce lower cooling rates than a water quench, these tool steels do not suffer as much from thermal stresses nor distortion as a water quenched material. Two alloys of note within these families are the O7 and A10 grades, both of which form graphite within their microstructure due to substantial carbon content and result in increased machinability and lifetime of these materials [2]. Type D steels also have extremely high resistance to abrasion which aids its ability to cold work other materials, but as a result these alloys are substantially more difficult to machine or grind [2].

Type P tool steels are alloys prepared specifically for plastic or die cast molds. A relatively low carbon content allows the alloys to be machined and shaped easily into molds and dies while in its annealed state. Once shaped appropriately, the tool steel is hardened through carburization which also serves to increase wear resistance [2].

Type H tool steels are a group of alloys with moderate levels of carbon and high amounts of carbide forming alloying elements, such as chromium, vanadium, tungsten, and molybdenum. Their resistance to impact loading, softening, and thermal fatigue at high temperatures is achieved by the formation of fine carbides within a moderately carbonaceous martensitic matrix, and makes these steels ideal for hot working tools. As with the O, A, and D tool steels, type H steels can also be air hardened [2].

Type T and M tool steels are tungsten and molybdenum high speed steels respectively. These groups, similar to type H, have substantial amounts of carbide forming elements which promote high temperature toughness for these materials. The microstructures for

these alloys contain large amounts of thermally stable carbides which also promotes wear resistance and high temperature hardness and makes these materials ideal for high-speed cutting tools. Type M tool steels have slightly higher toughness and decarburize more easily than type T steels, but both are otherwise the same [2].

1.1.2 Heat Treatments

While all tool steels may be heat treatable, their exact procedures can vary greatly. Type W tool steels are to be austinitized at 800°C and quenched in brine [4]. Types M and T require multiple isothermal holds, including a preheat at 730°C – 850°C, austenitization at 1200°C – 1300°C for 15 minutes, then tempering at 550°C for 4 – 6 hours [5]. Types S, O, A, D, and H follow a similar path as types M and T, requiring a preheat of 650°C – 800°C and austenitization at 800°C – 1250°C, but then being quenched in either air, oil, or brine depending on the particular alloy, before finally being tempered at 200°C or 550°C [3].

1.1.3 Microstructures

As discussed in the above sections, a typical hardened tool steel microstructure consists of iron and other alloy carbides within a martensitic matrix. High alloying element content aids in creating martensite during quenching [2]. The carbon and carbide-forming alloying element content determine the presence and type of carbides that form: the carbides formed in low alloy content tool steels are mainly cementite, which have an approximate hardness of 800 HV, whereas higher alloy content tool steels can have chromium, molybdenum, tungsten, or vanadium carbides, which can have an approximate hardness of 1400 HV. It is the amount and composition of the carbides within the martensitic matrix that provides tool steels with their characteristically high wear resistance [6].

In general, spherical shaped carbides soften the material, providing optimal machinability and formability for most tool steels at the cost of reduced hardness. More uniformity in

spheroidization can be achieved from a more uniform starting microstructure, which results in a softer annealed hardness. As the carbides coarsen and become more spheroidized, the bulk hardness of the steel continues to decrease. If the carbides become too coarse, carbon dissolution during austenitization is hindered. A uniform distribution of fine carbides is integral for minimizing grain growth during this process [6].

Carbides may take one of several stoichiometries depending on the presence and concentration of alloying elements. Cementite (Fe_3C) is the most commonly formed carbide as it primarily contains iron and carbon but is softer than other carbides and is readily dissolved during austenitization. Carbides of type MC follow a NaCl FCC structure and primarily consist of vanadium in tool steels, but can contain titanium, niobium, tantalum, or zirconium when present in other alloys. These are the hardest carbides, are highly resistant to dissolution during austenitization, and are typically present in high speed tool steels, particularly those with relatively high vanadium content [6].

M_2C carbides have a hexagonal crystal structure consisting primarily of molybdenum or tungsten but are relatively uncommon in tool steels except for some annealed grades. M_6C carbides form an FCC crystal structure and are also typically molybdenum or tungsten rich, although they can contain low amounts of chromium and vanadium. These carbides dissolve slowly during austenitization and are typically found in type T and M tool steels. M_7C_3 carbides are rich in chromium with a hexagonal crystal structure. They dissolve slowly into austenite during hardening and are usually found in type D tool steels. $M_{23}C_6$ carbides are chromium-rich, FCC phases typically found in high speed tool steels as well as 420 stainless steel [6].

Figure 1 shows the microstructure of a partially remelted and air quenched D2 tool steel. As explained in the relevant work, the large globular grains present in this SEM image were identified as ferrite and austenite, while the intergranular network along grain boundaries are primarily chromium and vanadium carbides [7].

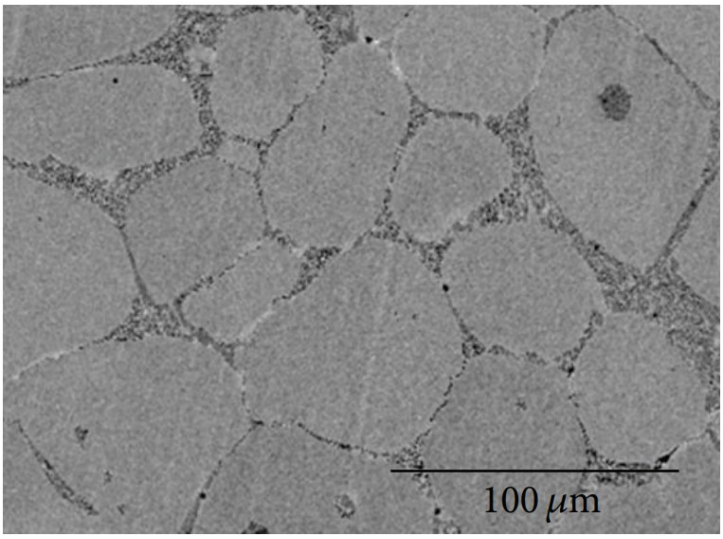

Figure 1 - An SEM image depicting the microstructure of partially remelted D2 tool steel [7].

Some tool steels, as discussed above, may contain graphite which increases the overall machinability of the material. This can be achieved by adding additional silicon to some tool steel chemistries. Sulfur has also been found to aid machinability, although this is typically avoided as it readily forms manganese sulfide which tends to decrease the material's toughness [6].

1.1.4 Mechanical Properties

The mechanical properties of tool steels can vary greatly between different types and even between alloys of the same type. In general, properties are relatively consistent within a group and only fluctuate a small amount. Table 2 provides a generalized overview of some key tool steel properties.

Table 2 - A simplified overview of the mechanical properties of various types of tool steels [2]

	Property					
Type	**Hardness, HRC**	**Machinability**	**Toughness**	**Softening Resistance**	**Wear Resistance**	**Crack Resistance**
W	50-64	Very high	High	Very low	Low	Low
S	45-60	Low	Very high	Low	Low	High
O	57-64	High	Low	Very low	Low	High
A	50-65	Low	Low	Medium	Very high	Very high
D	54-65	Very low	Very low	High	Very high	Very high
P	58-64	Low	Medium	Very low	Low	Medium
H	35-60	Low	Medium	Medium	Low	High
T	60-68	Low	Very low	Very high	Very high	Low
M	60-70	Low	Very low	Very high	Very high	Low

1.2 Binder Jet Printing Technology

Binder jet printing (BJP) is a type of additive manufacturing, or 3D printing, wherein a part is built from powder material on a layer-by-layer basis using an aqueous- or solvent-based binder to bind nearby powder particles together. Powders used in BJP are typically spherical in morphology and are in the range of 30 – 50 μm in size as they need to flow well enough to be easily spread over existing layers of powder without disturbing the previously printed layers [8]. The overall process from printing to fully dense part can be seen in Figure 2. The binder is ejected onto a flat bed of loose powder by following a predetermined set of parameters and directions to generate a loosely bound cross section of the build. A new layer of powder is then spread over the resulting binder-infused cross section and the process of binder ejection and powder spreading repeats until all layers have been printed. Once printing has finished, the powder bed and the produced parts are subjected to a curing and subsequent debinding thermal cycle to safely remove the binder and strengthen the parts while still maintaining their printed geometry. Fully de-bound parts are finally sintered at further elevated temperatures where, much like in traditional powder metallurgy, the parts undergo final densification and are further strengthened. At this stage, an infiltrating metal may be introduced to aid in the densification during sintering, though this is no longer a common practice due to the expensiveness and reduction in mechanical properties associated with adding

additional, different material to the existing composition. Further details on the many different facets of BJP technology are provided in the sections below.

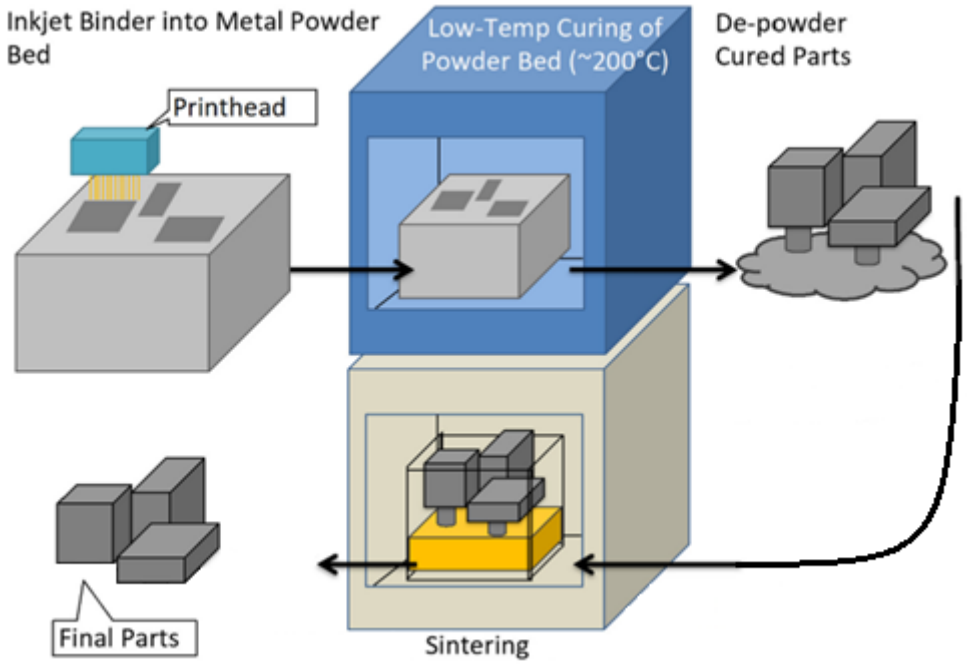

Figure 2 - A schematic showing key stages of BJP including printing, curing, de-powdering, and sintering [9].

1.2.1 Powder Feedstock Production

Powders used in AM, and in powder bed processes specifically, are typically spherical in shape with fine particle sizes and narrow size distributions [8]. These properties allow the powder to spread evenly and uniformly across the powder bed, providing layers of consistent thickness throughout the build.

In order to produce spherical particles with a small size distribution, most AM powders are produced via gas atomization, which is a relatively expensive process [8]. Water atomization has been examined as a potential cheaper alternative for producing AM powders, though the work in this area is minimal compared to AM research as a whole [8, 10, 11]. Powders produced via water atomization are typically coarser and more irregularly shaped than gas atomized powders, however it has been found that careful

adjustments to the atomization parameters can produce powders which are of a finer size and more spherical in shape [12]. A comparison between typical gas atomized and water atomized powders can be seen in Figure 3 below. As explained above, the gas atomized powder particles are highly spherical with relatively small particle size distributions, whereas the water atomized particles are more irregular and may vary in size to a greater extent.

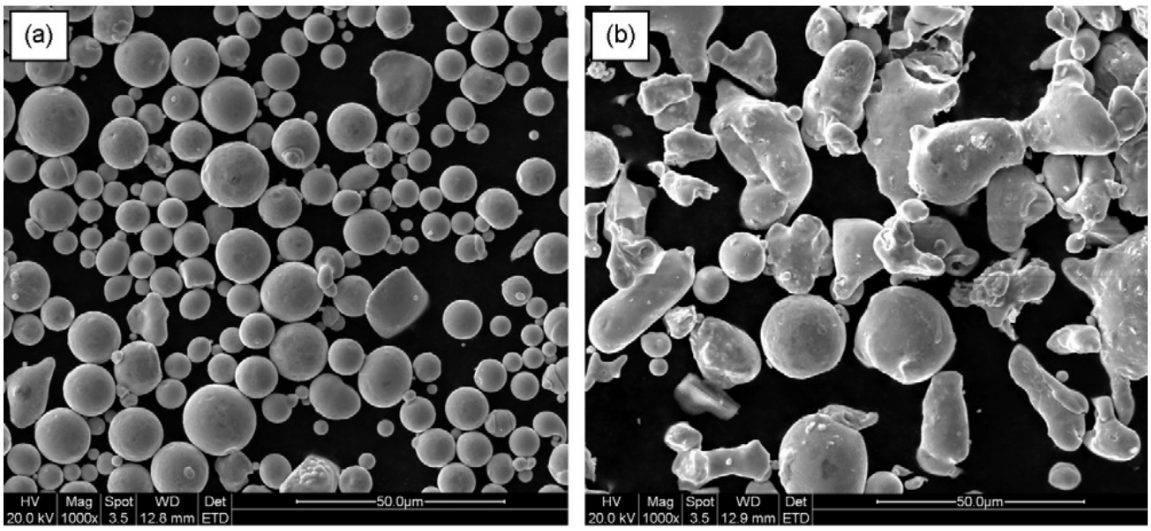

Figure 3 - SEM images showing the morphological differences between (a) gas-atomized and (b) water-atomized stainless steel powder [13].

1.2.2 Binder Systems

In BJP systems, binders serve to hold the powder particles together during printing and in the early stages of post-print heat treatments, after which the parts themselves gain sufficient interparticle strength to be handleable. A variety of binders exist for printing metals, ceramics, and polymers, though only those used with metals will be discussed in this work.

Binders used in metal BJP are primarily aqueous- or solvent-based and may contain smaller particles to aid in binding efficacy and sintering response. In these cases, the included nanoparticles melt at lower temperatures than the base material and aid in fusing

together nearby powder particles in the curing phase [14]. While there are several issues with particle containing binders, such as nozzle clogging in the printhead, there has been some work done in looking at particle-free binders which still precipitate metal nanoparticles during heating [9, 15]. Other binders which do not include, or precipitate metal nanoparticles typically contain a thermoset polymer which serves as a glue to hold the loosely bound particles together until it is later removed through volatilization. Figure 4 shows a comparison between nanoparticle containing binders and thermoset binders. While both the nanoparticles and thermoset polymers serve the same purpose of loosely holding the powder particles together, the nanoparticles provide more strength to the as-printed and green parts [15, 16].

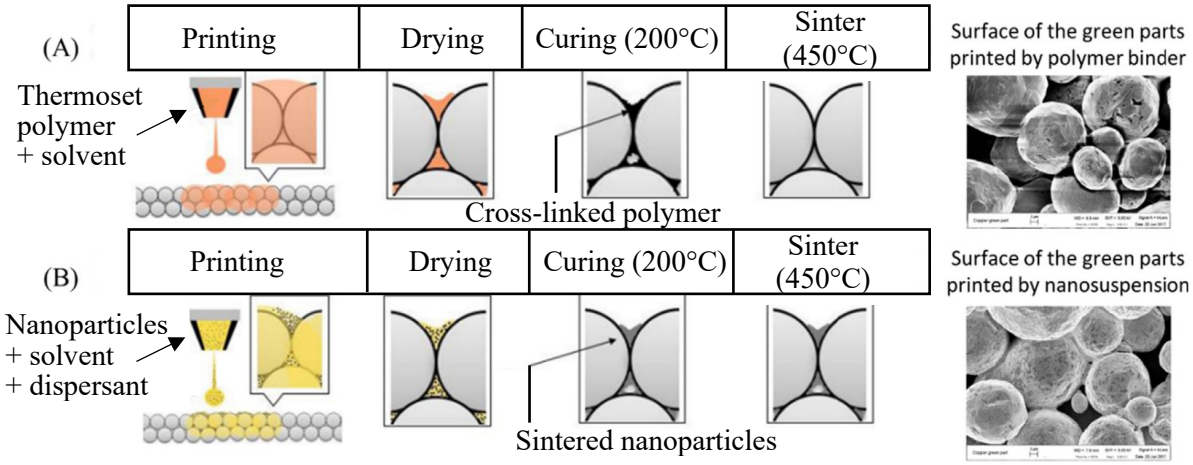

Figure 4 – A comparison between (a) thermoset polymer and (b) nanoparticle containing binders for BJP [9, 15].

In terms of general properties, a suitable binder would have low viscosity to prevent the liquid from sticking to the printhead as it is being jetted. A balance must be reached, however, as having too low of a viscosity or depositing too much binder may result in "binder bleed through", wherein the deposited binder saturates multiple layers at a time. This can often be avoided by adjusting printing parameters to account for the packing density of the powder such that only enough binder is deposited to permeate the topmost layer of the powder bed. As the binder must eventually be removed from the part, the binder should maintain a low boiling point and not off-gas harmful components [14].

1.2.3 Printing Concept

Binder jet additive manufacturing is a layer-by-layer method of printing. A simplified schematic of a binder jet printer is shown below in Figure 5. The general process involves a powder hopper or reservoir and powder spreading or rolling mechanism to deposit and spread an even layer of powder over the work area. This is usually repeated several times initially to form a stable substrate on which the printed layers will not move or drag. Once the bed has achieved a predetermined substrate depth, the printhead then deposits binder onto the top layer of powder, creating a single-layer thick cross-section of the product. The binder-infused powder is briefly heated to aid in drying the binder and binding the particles together before the work area lowers to allow a new layer of powder to be gently spread over the previous. This process is repeated several hundred times to create a fully bound product encased in loose, unbound powder. The presence of the loose powder surrounding the product provides support to the as-printed component and eliminates the need of support structures during printing that other methods of additive manufacturing often require.

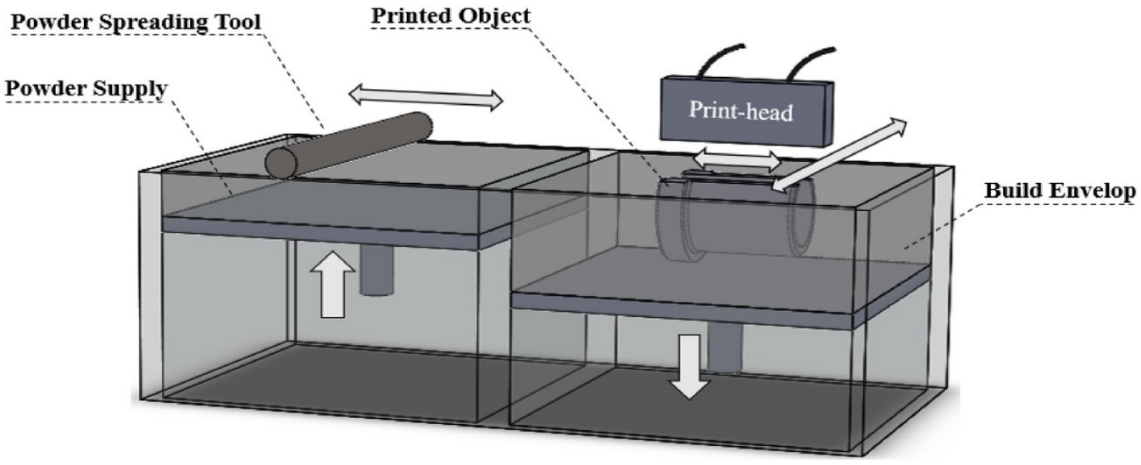

Figure 5 – A schematic of the binder jet printing process [14].

1.2.4 Curing and Debinding

Once a print has been completed, the job box containing both the bound parts and the loose powder is placed into a curing oven for several hours. This serves to remove some binder constituents and to polymerize others that subsequently strengthens the bonds between powder particles within the printed part. After curing, the parts may be removed from the powder bed by gently dusting away the surrounding loose powder as well as any loose powder remaining on the part itself or within any geometrical crevices. At this stage, the parts are in a proverbial "green" state, where they are sufficiently strong to be handled without the support of the powder bed but remain quite weak and fragile.

To further strengthen the parts, they are placed in a furnace for several hours and held at multiple isotherms to fully remove the remaining binder constituents and to aid in partially densifying the parts. This leaves the parts in a "brown" state, as they are notably stronger than the "green" parts but are still quite weak compared to a wrought counterpart of the same material due to the residual porosity left by the removal of the binder.

1.2.5 Sintering

Historically, two primary methods exist for densifying BJP parts, namely infiltration and sintering. Infiltration involves the use of an additional material with lower melting point than that of the material utilized in the printed part itself. This infiltrant is melted over the porous BJP part wherein the liquid then infiltrates the part, filling pores via capillary action. This eliminates the need to sinter the printed part at a much higher temperature, but due to the addition of a secondary material the original chemical composition of the printed part is altered [9]. Conversely, sintering is a means of providing sufficient thermal energy for the powder particles to physically bond. Ideally, this produces a strong, high density part that also maintains the required alloy chemistry. Porosity removal at this stage causes the part to shrink in all dimensions and may result in distortion. A comparison of these two densification processes is shown in Figure 6. In more recent years, infiltration has largely been abandoned as a densification process for BJP due to

the high cost associated with the infiltrant material as well as the relatively poor mechanical properties resulting from the addition of the infiltrant.

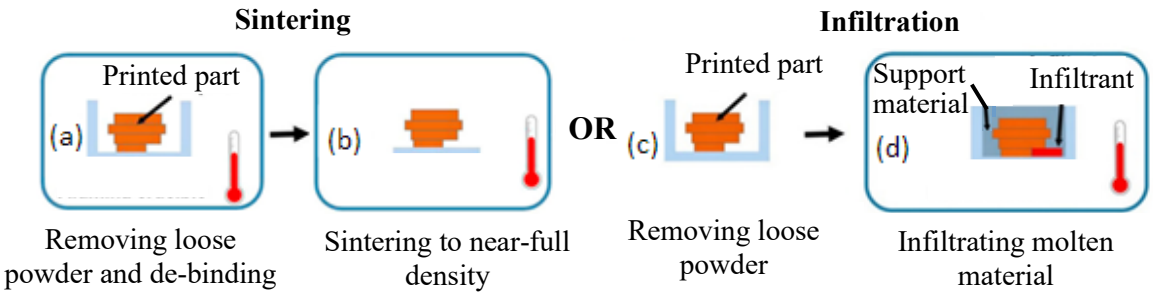

Figure 6 – The possible processes for achieving full or near-full density in a BJP part [9].

Depending on the material and the furnace temperature used, sintering may involve the formation of a temporary liquid phase to aid in densification. This is termed liquid phase sintering, whereas sintering without liquid formation is referred to as solid state sintering. The specifics of these sintering technologies are discussed below.

1.2.5.1 Solid State Sintering

Solid state sintering is, as the name would suggest, when a part is sintered in the absence of any solid to liquid phase transformations. Densification during solid state sintering occurs by mass transport between particles, and is driven by thermodynamic considerations that strive to achieve a net reduction in surface free energy [14, 17–19]. As smaller particles have higher surface energies, densification is enhanced with finer powders but ultimately, temperature is the most influential factor in terms of rate of densification as small changes in sintering temperature can greatly change the rate of diffusion and in turn, the speed of densification [14, 20].

In the initial stage of solid state sintering, bonds are formed between the loosely compacted powder particles via surface and grain boundary diffusion resulting in the formation of a neck between the two particles. At this stage, neck formation occurs independently throughout the entire part, but after sufficient formation and growth, necks

of neighboring particles begin to impinge. Volume transport mechanisms then become more prevalent, which aid in neck growth and decrease the distance between the now connected particles. This causes the part to shrink somewhat as the particles become closer together and facilitates densification [20].

Solid state sintering relies on diffusion to transport mass from one area of a particle to the space between it and another particle. Even at elevated temperatures, diffusion in and through a solid body is very slow compared to diffusion through a liquid, meaning bodies being sintered using only solid state sintering typically require higher sintering temperatures or more time at a given temperature in order to achieve an acceptable final density [20].

1.2.5.2 Liquid Phase Sintering

Liquid phase sintering (LPS) is a method of increasing the densification rate by partially melting the alloy during the thermal cycle. LPS also tends to produce denser parts, and can be applied to larger powder particle sizes [14]. During LPS, a liquid phase is present alongside solid particles and may be transient or may persist throughout the entire sintering process [21]. The liquid phase pulls the solid particles closer together through capillary action, thus enhancing the overall densification of the material [19, 21]. Furthermore, as diffusion rates are higher in liquids than in solids, the presence of a liquid phase also assists with the atomic movement of mass as needed for densification [22]. Once a liquid phase exists, there are three main steps in LPS (Figure 7). Contrary to solid state sintering, one of the early stages of LPS involves the rearrangement of solid particles which allows the particles to spontaneously move into a denser and more compact structure. Following this stage is solution-reprecipitation, wherein mass is transported from small grains to large grains through the liquid due to the higher solubility of fine grains than coarser grains in the existing liquid phase. This mass transport results in overall densification of the material by means of eliminating smaller grains and the coarsening of larger grains. As the grains continue to coarsen, their overall shape also changes to better accommodate pore removal and final densification [21–24]. The microstructure resulting from LPS typically contains larger grains which remained

solid throughout sintering and coarsened through the solution-reprecipitation stage alongside an intergranular network of the solidified liquid phase [19]. Extended sintering in the presence of the liquid phase can cause grain coarsening and an overall decrease in mechanical properties [19].

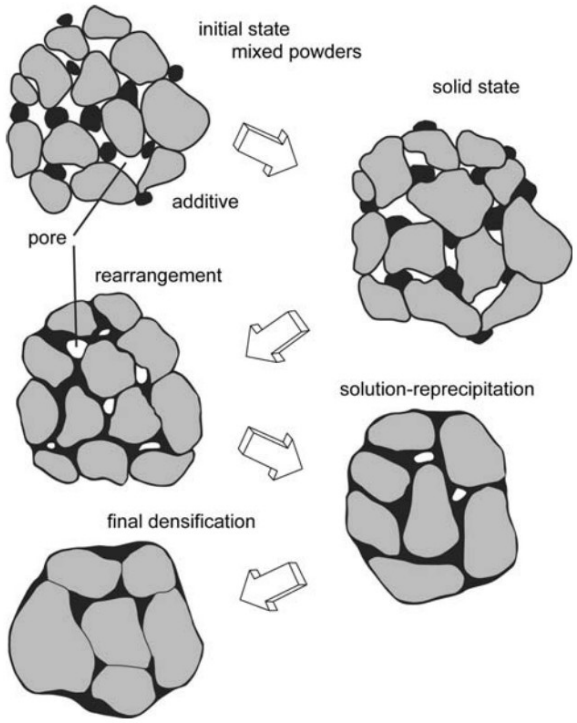

Figure 7 - A depiction of liquid phase sintering [22].

LPS is aided by the particle size and wettability of the liquid phase on the solid particles [19]. The initial rearrangement stage of LPS in particular benefits from a high degree of wettability as this allows the liquid to spread and cover more solid particle surfaces, thus providing both lubrication and capillary forces for grain rearrangement [19].
Furthermore, a wetting liquid will preferentially flow to contact smaller grains and pores in order to achieve the lowest possible energy condition. Capillary and contact forces between smaller, wetted grains can achieve stresses comparable to those produced in some pressure-aided sintering processes, such as hot isostatic pressing, which further promotes rapid densification [22]. Conversely, a poorly wetting liquid will retreat away

from solid particle surfaces, resulting in swelling of the part rather than densification [22].

LPS can occur when sintering a compact composed of two or more powders of different chemistries, resulting in the melting of one component or through the formation of a eutectic phase [21]. The other method of triggering LPS, which, unlike the previous, can be applied to prealloyed powders involves heating them to a temperature between the liquidus and solidus temperatures of the alloy [21]. This temperature range is often referred to as the 'mushy zone' and the process is then termed 'supersolidus liquid phase sintering' (SLPS), as the material enters a soft, semi-solid state [19].

For SLPS, densification occurs primarily through the viscous flow of these semi-solid particles aided by capillary forces in the liquid. Densification speeds increase with more liquid content due to the overall reduction in viscosity of the semi-solid particles, though distortion is more likely to occur at these lower viscosities. As a result, optimal SLPS sintering temperatures for full densification without distortion are generally within a relatively narrow window [19]. Ideally, SLPS should be performed at a temperature wherein 10% - 40% of the microstructure is liquid and 80% - 90% of the surface area of solid particles are wetted by the liquid phase in order to promote rapid densification without significant distortion [19].

In SLPS, the liquid phase may also form from within powder particles, in which case the corresponding particles are fragmented into smaller individual grains. As discussed previously, smaller grains promote rapid densification due to the associated elevated contact forces, so the fragmentation of larger particles due to internal liquid can allow even particularly coarse powders untenable to LPS to sinter well through SLPS [19, 25]. In this manner, virtually any powdered alloy, regardless of particle size, can be sintered through SLPS so long as it has a mushy zone and a wetting liquid.

1.2.6 Post-Sintering Operations

One of the largest disadvantages of BJP is the amount of post-printing processing that must take place in order to achieve optimal mechanical properties and desired

dimensional tolerances. So far, several post-printing operations have been discussed which altogether contribute to binder removal and densification of the printed part. Depending on the material and the densification method used, various post-sintering operations may also be considered or necessary for further improving the physical, mechanical, and geometrical properties.

Heat treatment can be performed to maximize mechanical properties or to obtain specific, desired properties. Various heat treatment profiles have been discussed above for different tool steels, but overall these treatments serve to maximize strength and hardness of the particular alloy. These heat treatments reduce any stresses or dislocations present and can be used to specifically tailor the microstructure to suit the needs of the product.

As discussed above, BJP products generally experience significant amounts of shrinkage during sintering which may not occur uniformly throughout the entire part depending on the complexity of the geometry and localized variations in green density. In these cases, it may be desirable to oversize the part during printing such that excess material on the post-sintered, distorted product can be machined away to achieve the desired geometry. Figure 8 demonstrates this shrinkage in two nickel superalloy tensile specimens.

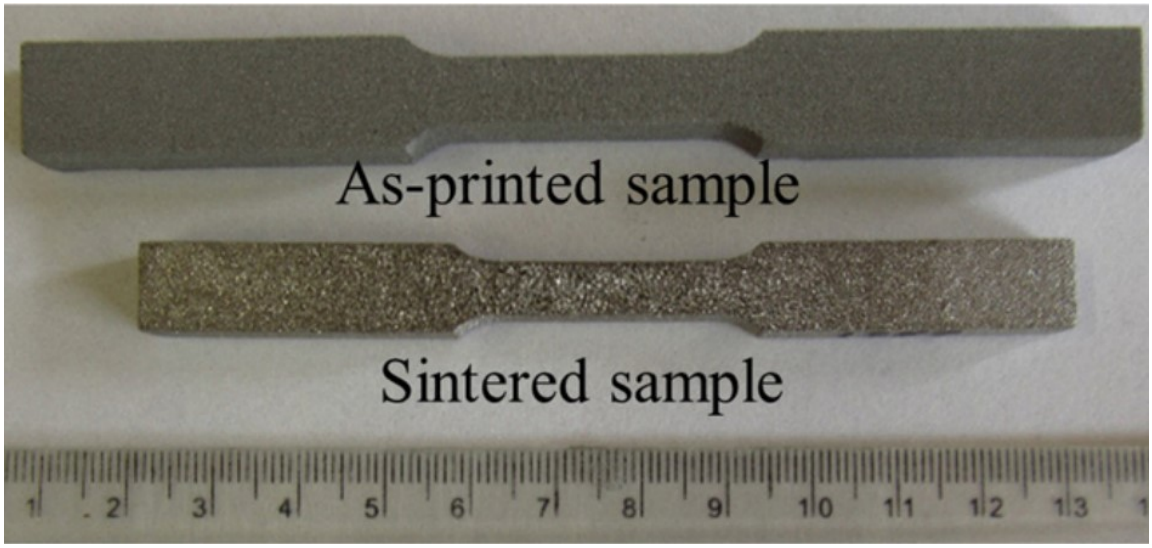

Figure 8 – Size comparison between an as-printed and sintered sample of Ni-based superalloy 625 [26].

Even BJP parts which do not experience significant distortion during the various thermal profiles may require some surface machining. One study found that the average roughness of BJP parts is 6 μm, so surface finishing is sometimes implemented as a post-sintering operation. The two most commonly used finishing methods for BJP parts are bead blasting and tumble polishing, which can reduce the surface roughness down to 7.4 μm and 1.25 μm respectively [9]. Alternatively, a smoother surface can be achieved without surface finishing by using a finer powder during printing. With a finer input powder, the layer size can be decreased which directly leads to a reduction in surface roughness of the printed part.

1.3 Commercial Binder Jet Materials

The main powder characteristics that must be considered when choosing a material for powder bed based AM systems are the flowability and packing density of the loose powder [27]. The flowability of the powder determines the ease in which each successive layer can be spread, so an ideal powder would have high flowability to prevent agglomerates or voids. To achieve this, AM powders are typically spherical in shape with a narrow range of particle sizes, ranging between 30 to 50 μm for most powder bed applications [8]. As discussed above, finer particle sizes may be used to achieve thinner layer thicknesses, which ultimately produces parts with smoother surface finish and higher accuracy in printed details. The main disadvantage to using fine powders is that they are more susceptible to interparticle forces such as friction and electrostatic forces which negatively impact the flowability of the powder and, therefore, the overall print quality [8].

The packing density of the loose powder affects the green and brown part density, and ultimately affects the overall shrinkage of the part. A more densely packed powder will suffer less overall shrinkage than a loosely packed powder, and will tend to achieve higher final densities [8].

Compared to other powder bed AM systems, such as laser powder bed fusion or selective laser melting, BJP does not rely on melting the powder to create a printed part. As such,

BJP may be used in conjunction with powders that are difficult in PBF, such as certain refractory materials or those with high melting points. Virtually any powder can be used in BJP, however like all metal AM processes, BJP is severely lacking in terms of materials research [9, 14]. Common materials that have been researched using BJP include ceramics, metal matrix composites, Inconels, and stainless and tool steels [9].

1.4 Applications for Binder Jet Printing

BJP is the only powder bed AM process that does not involve complete melting of the parent material [14]. By printing at significantly lower temperatures than fusion-based PBF systems, BJP parts can avoid certain issues such as residual stresses due to large thermal gradients, oxidation, and elemental segregation [9]. This leads BJP parts to applications where such issues would be detrimental or harmful, such as engine parts or electronic devices [28, 29].

As discussed previously, virtually any powdered material can be used in BJP, whereas PBF systems are limited in that they cannot make use of refractory or high melting temperature materials [9]. As well, since BJP is not limited by laser scan speeds, it typically has higher production rates than PBF systems making it an ideal system for rapid prototyping and even moderate volume production. BJP can also produce finer details and more complex geometries than any other AM system [9]. For example, the titanium carbide parts shown in Figure 9 would be difficult or impossible to produce through conventional methods due to the complex geometry and thin walls, and other AM processes would not be able to achieve a melt pool due to the high melting point of the material.

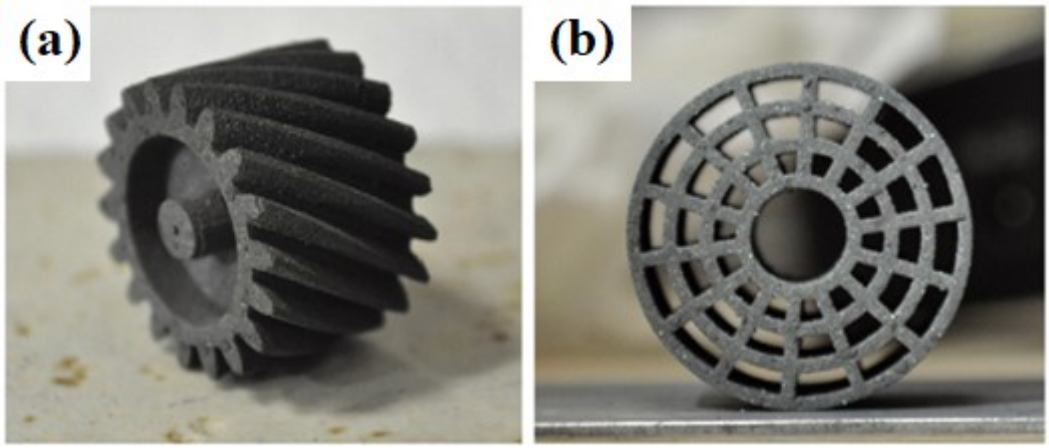

Figure 9 – BJP titanium carbide parts with complex geometries, (a) helical gear and (b) "spider web" lattice truss [30].

While PBF systems typically require support structures for ensuring stability when printing parts, BJP does not. The presence of loosely packed powder surrounding the bound parts provides sufficient strength to support the parts throughout printing and curing, after which they become strong enough to be handled outside the powder bed [9]. This allows for easy recycling of the unbound powder, as it has not been thermally nor chemically altered. Furthermore, BJP parts typically need little to no machining, whereas other PBF systems would require removal of supports, meaning BJP produces less material waste than PBF.

One of the major benefits of BJP and AM in general is the ability to prototype and improve upon existing mechanical assemblies. Mechanical assemblies of parts, which would traditionally require the production and assembly of multiple parts each with their own post-processing steps, can often be redesigned for AM such that multiple parts are combined into a single component with more complex geometries [9]. General Electric, for example, has printed a redesigned version of an old helicopter engine which reduces the assembly of 900 individual parts down to 16, as well as reducing weight and cost of the engine by 40% and 60% respectively [31]. These sorts of redesigned prototypes are ideal for BJP as it allows for a high level of geometrical complexity which would not otherwise be possible to manufacture.

Other applications of BJP include jewelry, food technology, sand casting molds, waveguide circuits and antennas, concrete construction, renewable bio-based materials, bioceramic scaffolds, bio-polymers, sandstone production, complex gear cases, fuel tanks, transmission housings, structural hinges, and biomedical applications and drug delivery systems [9, 28, 32–41]. Some research has also shown the potential for BJP produced electrochemical energy storage systems in the near future [42].

To date, BJP has been used to produce many metal products within a variety of industries. Several varieties of tool steels have been used to produce tooling and dies for manufacturing purposes, such as the H13 extrusion die for plastics shown in Figure 10(a) [43]. Furthermore, various types of automotive parts have been produced via BJP, including pistons and piston heads, clutch plates, power steering joints, and, as shown in Figure 10(b), a 316L stainless steel thermostat housing replacement for a vintage Mercedes Benz [44]. These parts often have complex geometries typically requiring either casting in specialized molds or hours of machining to produce but can be easily created through BJP. The part shown in Figure 10(b) is of particular interest as it is a part which has historically been cast but has become unavailable in recent years due to its mass manufacturing being discontinued [44]. In this sense, BJP allows the user to produce specific, custom-made parts tailored to the needs of the user. Other custom-made metal products produced via BJP include jewellery, guitar tailpieces, and golf club parts, such as the 17-4 PH stainless steel putter head shown in Figure 10(c) [45]. Thanks to the high level of customizability and ease of producing complex geometries in BJP, parts of this nature can be designed and printed with the user in mind, in this case with a specialized putter head design which may distribute the weight to better suit the playstyle of the user.

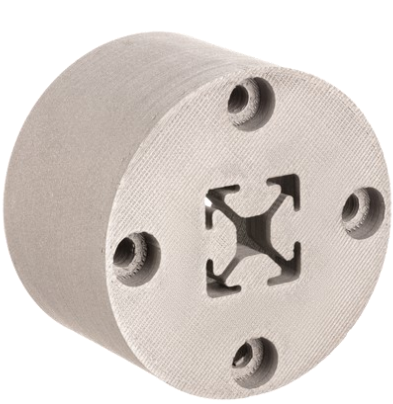

(a)

(b)

(c)

Figure 10 – Several examples of metal parts produced via BJP. (a) An extrusion die used in plastic extrusion, shown here composed of H13 tool steel [43]. (b) A thermostat housing replacement for a vintage Mercedes Benz engine, shown here composed of 316L stainless steel [44]. (c) A custom-made putter head for golf clubs, shown here made from 17-4 PH stainless steel [45].

CHAPTER 2 – RESEARCH OBJECTIVES

As discussed previously, most powders used in AM are produced via gas atomization in order to achieve good flowability due to the fine particle size and highly spherical morphology [8]. Gas atomization is a relatively expensive process, however, especially in comparison to water atomization. The primary downside to water atomization is the coarse particle size and irregular particle shape typically produced through this method, though some research on water atomization has found that particles of finer sizes and more spherical in shape can be produced [12].

Accordingly, the main objective of this research is to investigate the feasibility of using water atomized powders in binder jet additive manufacturing. More specifically, this would entail the production of a printed part with minimal porosity and distortion, as well as showing relatively similar mechanical properties to the wrought counterpart material. The particular alloy selected for this research is a water atomized D2 tool steel powder as tool steels are an alloy system with relatively little research in BJP to date [46]. To achieve these objectives, this work focuses on optimizing key parameters throughout the various stages of the binder jet printing and post-printing processes for the aforementioned D2 tool steel powder.

Assessment of the printing, curing, de-binding, and sintering stages of printing are evaluated based on the measured sinter density of samples as well as visual inspection for any noticeable distortion. Heat treatment effectiveness is to be determined by heat treating wrought and sintered BJP samples of similar alloy composition under the same heat treatment procedure and measuring the resulting hardness and compressive data. Microstructural analyses are also performed at key stages of the post-printing processes to provide qualitative insight into the behaviour of the material and development of the microstructure.

CHAPTER 3 – BINDER JET PRINTING OF A LOW-COST TOOL STEEL POWDER

R.D. Ley[1], I.W. Donaldson[2], D.P. Bishop[1*]

1-Dalhousie University, Dept of Mechanical Engineering, 1360 Barrington Street, Halifax, NS, Canada, B3H 4R2
2-GKN Sinter Metals, Advanced Engineering, 1670 Opdyke Court, Auburn Hills, MI, USA, 48326
* *Corresponding author* – Paul.Bishop@dal.ca*; +1.902.494.1520*

Paper is currently awaiting submission for publication in Powder Metallurgy

Abstract

Water atomization is a commonly used process to inexpensively produce large volumes of powders for press-and-sinter powder metallurgy. While the resulting powder particles are typically irregularly shaped and relatively coarse, adjustments to the atomization parameters can yield particles that are finer in size and nominally spherical, thereby facilitating their potential for application in additive manufacturing (AM). Thus, the objective of this research was to investigate the viability of water atomized D2 tool steel powder in the context of binder jet printing (BJP). Builds were printed, cured, de-bound, and sintered under various conditions to assess densification behaviour. Optimal sintering conditions for maximum density (98.5% theoretical) without significant distortion or grain coarsening were determined to be 1250°C for 30 min under high vacuum. Printed samples underwent a standard heat treatment process for wrought D2 and performed comparably to the wrought counterpart in terms of hardness (6.6% lower) and compressive elastic modulus (0.5% lower) with offset yield stress showing the largest difference (12.2% lower). Heat-treated BJP samples retained key microstructural features imparted by the printing process such as carbide clusters within large grains and intergranular lamellae of eutectic carbides and prior austenite, whereas the wrought microstructure was largely homogenous with fine grains and carbides.

Key Words: Additive manufacturing, water atomization, binder jet printing, D2, tool steel, sintering

3.1 Introduction

Additive manufacturing (AM) of metallic materials has seen significant growth since its development within industrial and research settings [47, 48]. In general, AM processes serve to consolidate a given material into a geometrically complex product with minimal internal porosity [49]. Materials utilized in AM are typically polymeric, metallic, or ceramic but other less conventional systems such as paper and even chocolate have also been utilized [48, 50]. In contrast to traditional manufacturing methods which remove material from a workpiece to achieve a desired shape, AM builds a part directly from the feedstock material into the final geometry in a near-net-shape manner. In this sense, AM is a "green" production method as it requires minimal, if any, post-build machining and the unused feedstock can be repurposed for another print [49, 51].

In the context of metallic part production, a range of AM technologies exist. While these share the commonality of a layer-by-layer production process, they differ in terms of how the individual layers are created and bonded together [52]. Some methods, such as directed energy deposition (DED) and selective laser melting (SLM) use high powered lasers to locally melt powder particles together, in a way similar to laser welding [53]. While these processes can be largely automated from feedstock to fully dense product, they do tend to produce relatively high residual stresses in the part due to high cooling rates and as a result tend to require built-in support structures [9, 46, 47, 50]. It is also notable that DED products have a relatively rough surface finish that typically mandates machining prior to in-service use [54, 55]. Binder jet printing (BJP), on the other hand, forgoes the use of lasers altogether during printing. As such, materials that are laser-reflective and/or refractory in nature can be readily printed and protective atmospheres are not required at this stage of the cycle [50]. In addition, BJP maintains a relatively short printing time compared to other AM processes, support structures are not required during printing, and the sintered products exhibit an excellent surface finish as well as minimal residual stress. As such, BJP has been viewed as one of the most cost-effective AM processes for producing parts with complex geometries [49, 56].

A variety of metallic materials have been processed successfully via BJP including ferrous, nickel, and copper alloys [46, 48]. Ferrous alloys have been particularly well-

researched [8, 9, 46, 50, 56–68]. Focal points have included stainless steels [8, 56–61, 67, 68], pure iron [64, 65], tool steels [9], and biodegradable ferrous alloys such as Fe-Mn-Ca/Mg [62, 63].

The printing process in BJP is similar in some ways to conventional inkjet printing, but rather than printing in two dimensions on a singular sheet of paper, BJP prints on a multitude of thin powder layers successively to build a three-dimensional part. The printer itself contains three principal components: the powder bed, the powder delivery system, and the printhead. The printhead drops a solvent binder onto specific areas of the powder bed to create a loosely bound cross-section of the printed part [69]. The powder bed then moves down a layer and the powder delivery system provides and spreads a new layer of powder over it. The printhead prints the next cross section onto this layer of fresh powder and the process repeats, ultimately building the product by stacking and binding successive cross-sectional layers together [12]. Once printed, the binder must be cured in a furnace to strengthen the product to facilitate its removal from the powder bed. It is then heated again to a higher temperature to remove the remaining binder residue, leaving behind a "brown" part which has adequate strength for handling but is still highly porous [50]. To enhance density and overall metallurgical quality, the "brown" part is then sintered at a higher temperature in order to properly bond the powder particles together [69]. Alternatively, infiltration with a secondary metal, typically bronze, may be used after sintering as a means of reducing porosity while maintaining the geometry of the as-printed part [60, 70].

The feedstock utilized in BJP is comprised of fine (<20μm), spherical particles that are spreadable and conducive to post-print sintering [8, 47]. Powders of this nature are typically produced through relatively expensive processes, such as gas atomization, rotary atomization, or plasma-based technologies. An alternative technology is water atomization [8, 12, 69]. This method produces powder at an appreciably lower cost, but the particles are often irregularly shaped which suggests that they are not necessarily optimal for BJP [1, 8, 10]. However, with appropriate adjustments to water atomization parameters, the resulting particles can be tailored to be fine in size and more spherical/rounded in morphology as is desired for BJP [12]. As such, the objective of this

research was to investigate if a water atomized D2 tool steel powder was amenable to BJP. This included experimental work at all stages of the production cycle coupled with a comprehensive metallurgical assessment of the finished product, its response to heat treatment, and a direct comparison between it and conventional wrought D2.

3.2 Materials

The raw material utilized in this research was a water atomized (WA) D2 tool steel powder produced by GKN Hoeganaes. Samples of wrought D2 were also acquired for comparison purposes. The bulk assay of each material was measured using inductively coupled plasma optical emission spectrometry (ICP-OES) in a Varian Vista-PRO ICP-OES Chemical Analyzer. Carbon and sulphur contents were measured using an Eltra Elementrac CS-i analyzer while those of oxygen and nitrogen were determined through inert gas fusion using an Eltra Elementrac OHN-p apparatus. Measured chemistries for the raw materials coupled with the chemical specifications for wrought D2 are shown in Table 3. All elements present were within or near their target composition.

Table 3 – Composition of the WA D2 powder utilized (all values in weight %) as compared to the chemical specifications for wrought D2 [1].

Material	Fe	Cr	C	V	Mo	Si	Mn
Spec.	Bal.	11-13	1.4-1.6	≤1.1	0.70-1.2	≤0.60	≤0.60
WA-D2	Bal.	12.9	1.61	0.76	0.72	0.30	0.20

Particle size distribution (Figure 11) was measured via laser light scattering using a Malvern Master Sizer 3000. The material exhibited D10, D50, and D90 values of 14μm, 30μm and 58μm respectively. This size distribution can allow smaller particles to reside in the voids between larger particles, thus aiding the packing and densification of the powder. This size distribution can be seen in more detail in the SEM images shown in Figure 12. The powder morphology comprised a mixture of spherical, rounded, and rounded/irregular powder particles.

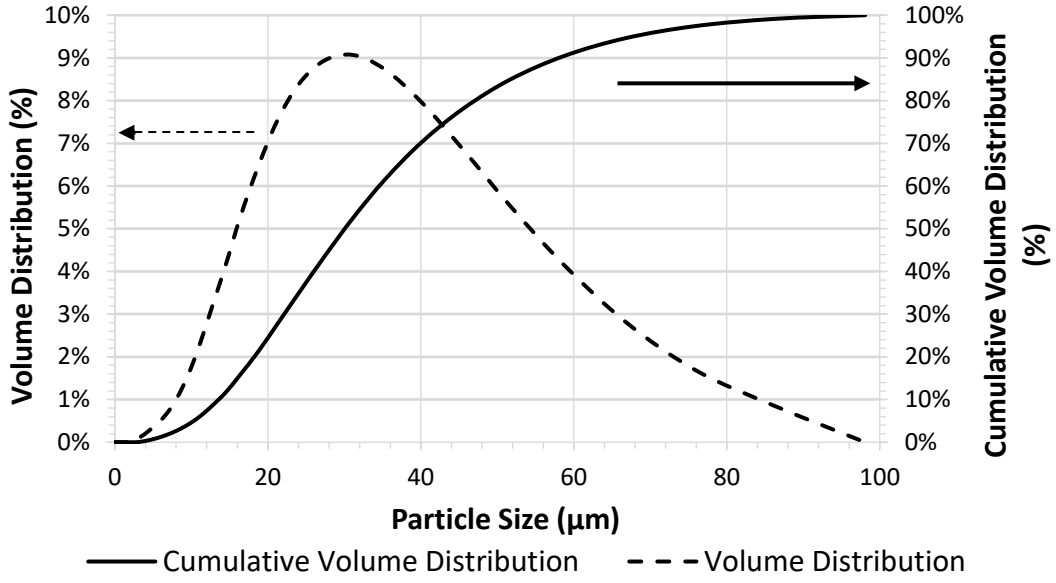

Figure 11 - Particle size distribution measured for the WA D2 powder.

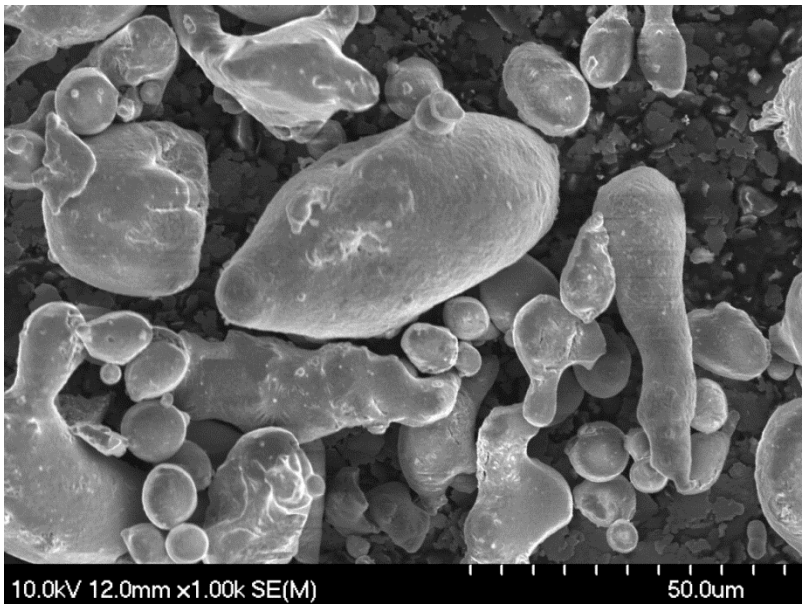

Figure 12 – Morphology of the WA D2 powder.

Powder bed density was measured by printing several open top, hollow cubes with internal dimensions 12.5 x 12.5 x 12.5 mm. These boxes were cured within the powder bed as usual, which ensured that they would not collapse or lose any contained powder.

After curing, the mass of the powder contained within each box was measured and the powder bed density was calculated using the known internal dimensions. Based on the results of six printed and cured cubes, the average powder bed density was calculated to be 4.37g/cm^3.

3.3 Experimental Techniques

BJP samples were produced using an ExOne Innovent+ binder jet printer equipped with AquaFuse aqueous binder. Printing parameters were adjusted from default settings to allow complete, even powder spreading across the bed. Parameters which remained fixed throughout this work included a layer thickness of 50 μm, desired binder saturation of 55%, powder packing rate of 60%, and a powder bed substrate comprising of 10 layers. After printing, the job box was placed in a Thermo Scientific Heratherm OMH Advanced Lab Oven to cure the binder at 180°C for 12 hours. Samples were then de-powdered, removed from the job box, and transferred to a Carbolite Three-Zone tube furnace for de-binding. Prior to heating, the de-binding furnace was evacuated and backfilled twice with UHP nitrogen (99.999% purity) after which it was evacuated once more so as to maintain a vacuum atmosphere for the duration of the de-bind cycle; heating to 600°C, hold for 2.5 hours, and furnace cool.

Preliminary studies on sintering response commenced with differential scanning calorimetry (DSC) and thermal dilatometry tests. The former were completed using a Netzsch 404 F1 Pegasus DSC. Calibration was completed by running a prescribed heating profile with an empty alumina crucible alongside the empty alumina reference crucible allowing the heat effects from the crucible to be subtracted from the data. DSC was completed on cured/de-bound disks (3mm diameter and height) and loose powder (20mg). The DSC was evacuated to $<5 \times 10^{-5}$ mbar and backfilled with UHP argon (99.999%) prior to heating at 10°C/min to the temperature of interest. For dilatometry, a Netzsch model 402C dilatometer was used to heat cured/de-bound cylindrical samples (6mm in diameter and length) under high vacuum (10^{-6} mbar) at 10°C/min to temperatures between 1000°C and 1300°C for different hold times. The system was calibrated for each heating profile with an alumina cylinder of the same dimensions.

After sintering in the dilatometer, samples were examined visually for distortion and their density was measured using the Archimedes principle [71]. The samples were then sectioned, mounted, and polished using a Struers Tegramin-20 auto-polisher according to standard metallography procedures. This included four sequential grindings consisting of 2 minutes 20 seconds on 220 grit SiC grinding pad with water as a lubricant, 4 minutes 30 seconds on MD-Largo grinding pad with DiaPro Largo 9µm diamond suspension as a lubricant, 4 minutes 30 seconds on MD-Dac polishing pad with Diapro Dac 3µm diamond suspension as a lubricant, and 2 minutes on MD-Chem polishing pad with OP-S 0.25µm silica suspension as a lubricant. Select samples were etched by submerging in a 5% Nital (5% HNO_3, 95% CH_3COOH) solution for 10 seconds. Microstructures were examined through use of a Zeiss Axiotech upright optical microscope and a Hitachi Cold-Field Emission S4700 scanning electron microscope (SEM) operated at 20kV and 10µA using the lower secondary electron detector. Energy dispersive spectroscopy (EDS) was performed on several locations of interest to examine and record the elemental distribution within the samples.

Transverse rupture strength (TRS) bars (6.35mm x 12.5mm x 31.5mm) and compressive strength cylinders (13mm diameter x 39mm length) needed for mechanical testing and heat treatment studies were then printed, cured, and de-bound in accordance with the procedures described earlier. These samples were sintered for 30 minutes under high vacuum (10^{-6} mbar) in a Bell Jar Furnace (Materials Research Furnaces, NH, USA) at various temperatures. Several sintered samples were selected to undergo a generalized heat treatment as described in ASTM A681 – 08 [4]. Here, samples were first austenitized in a Lindberg/Blue BF51866A-1 Box Furnace at 1010°C for 15 minutes, air cooled to 60°C, then tempered for 2 hours at 204°C in a Thermo Scientific Heratherm OMH oven. Hardness and compression tests were completed on heat-treated and non-heat-treated samples. The former was performed using a Wilson Rockwell 2000 Hardness Tester calibrated to the HRC scale and followed the ASTM E18 – 22 standard [72]. The latter was performed in an Instron 200HVL Hydraulic Frame equipped with a 50kN load cell under the conditions outlined in ASTM E8 – 19 [73]. Each specimen was compressed at 300MPa/min until the 0.2% offset yield stress was surpassed.

3.4 Results

3.4.1 Sintering Response

3.4.1.1 Thermodynamic Assessment

To amass a preliminary sense of the phases present as functions of temperature and composition, thermodynamic modelling was implemented. Here, the measured chemistry of the starting powder (Table 3) was considered with variations in carbon content. Figure 13 shows the pseudo-phase diagram for this specific D2 powder composition from 500°C to 1500°C. Carbon content was varied along the x-axis with a dashed vertical line shown at the measured concentration within the powder (1.6%). According to this diagram, several phase transformation events occur within this temperature window. Below 500°C there is a partial ferrite to austenite transformation which, on heating, reverts back to ferrite at 680°C. The final ferrite-austenite transformation occurs between 795°C and 810°C. The primary carbides present within the material, namely $(Fe, Cr, Mo)_{23}C_6$ ($M_{23}C_6$) and $(Fe, Cr, V)_7C_3$ (M_7C_3), dissolve into solid solution at 1072°C and 1235°C respectively. Finally, the predicted temperatures for the solidus (1197°C) and liquidus (1385°C) were also indicated. The amount of each phase present within this 500°C to 1500°C range is shown in Figure 14. Key features include the ferrite to austenite transition, carbide stability/dissolution, and liquid phase emergence. The latter is shown in greater detail in Figure 14 (b). Such data can be particularly helpful in a context of liquid phase sintering (LPS). Here, a small, but controlled amount of liquid is sought as it can significantly intensify and accelerate the densification process. However, the amount of liquid present may vary dramatically over a relatively small temperature range and can thus cause slumping or distortion if the temperature is not carefully controlled [19, 21, 25]. Previous studies on LPS report a typical desired liquid volume of ~30% for rapid densification, which should occur in the D2 powder at ~1254°C in accordance with the data shown in Figure 14(b) [25].

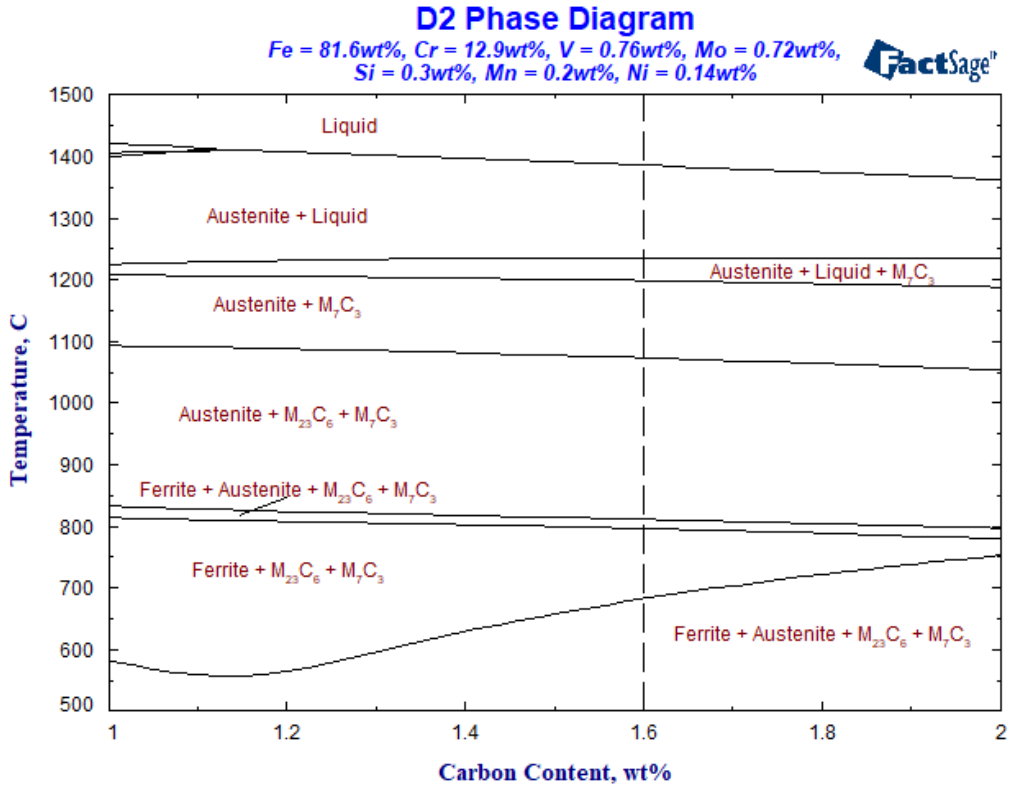

Figure 13 – Pseudo-phase diagram generated in FactSage for the measured D2 composition with varying carbon content.

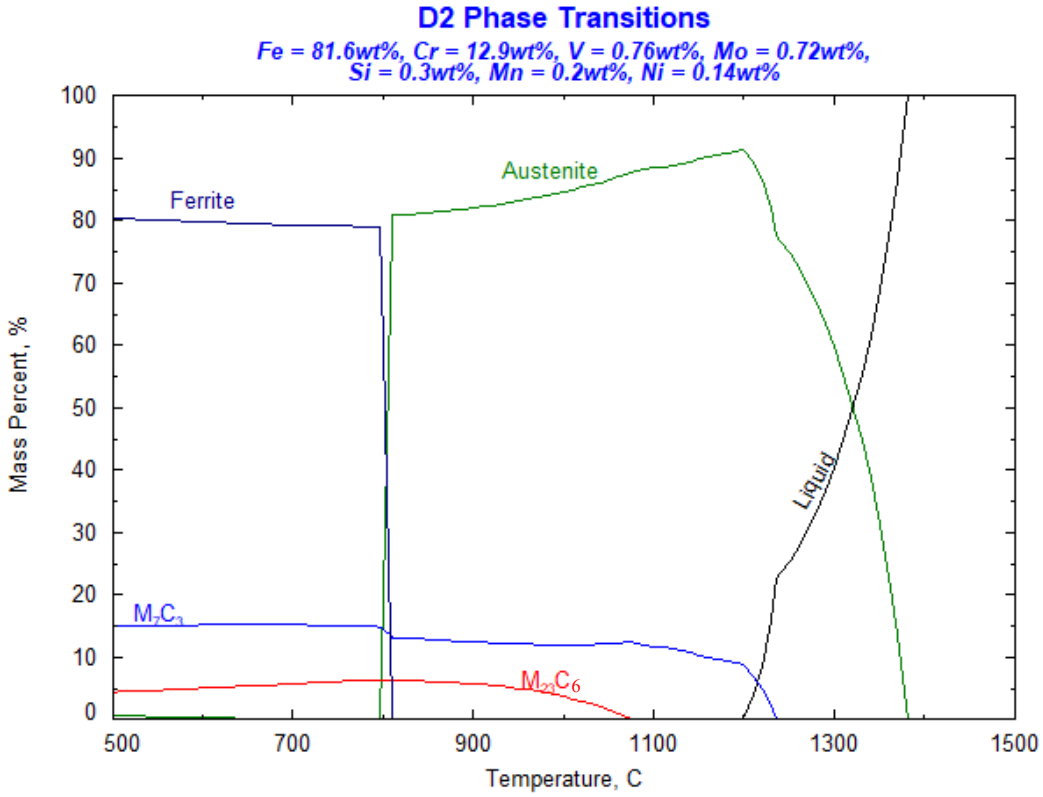

(a)

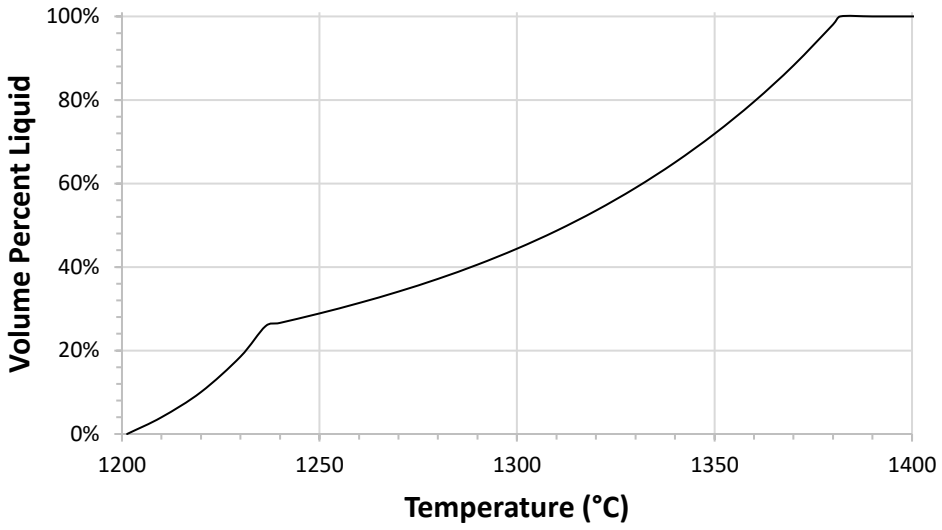

(b)

Figure 14 – Thermodynamic data for the D2 system illustrating (a) various phase transitions predicted to occur on heating from 500°C to 1500°C and (b) a more detailed view of the liquid phase evolution.

3.4.1.2 Thermal Analysis

Results from DSC tests on the as-received powder when heated to and cooled from 1400°C are shown in Figure 15. Five clearly distinguishable thermal events occurred during heating with only two reappearing on cooling. Through use of the phase diagram in Figure 13, these thermal events can be attributed to specific phase transformations. At 620°C, the onset of an exothermic peak labelled A was attributed to the transformation of martensite present in the rapidly solidified powder to austenite based on similar DSC work by Bombac et al. [74]. An endothermic event labelled B occurred at 840°C that was relatively well aligned with the predicted transition of ferrite into austenite (810°C) and was also in agreement with the work of Bombac et al. [74]. Two more endothermic peaks, denoted as C and D in Figure 15, began at 970°C and 1240°C and were attributed to the dissolution of $M_{23}C_6$ and M_7C_3, respectively. While peak D matched up well to the corresponding M_7C_3 dissolution peak in the work of Bombac et al., the dissolution of the $M_{23}C_6$ carbide differs by nearly 300°C. This appears to be due to the difference in material composition, as their similarly generated Figure 14 shows $M_{23}C_6$ dissolving completely by 780°C whereas here it is delayed to 1070°C. This is further backed by the work of Pirtovsek et al. where it was reported that higher amounts of Cr increase the precipitation temperature of eutectic carbides [75]. Additionally, since melting should begin at approximately 1200°C according to Figure 13 and Figure 14, it is likely that peak D may also represent incipient melting of the material. As a result, the apparent exothermic event which occurred between peaks D and E may instead be a gradual change in the baseline of the DSC trace as the heat capacity of the material changed due to the increasing amounts of liquid present. Therefore, the final thermal event during heating, labelled E, was instead an endothermic event which began at 1385°C and would have completed above 1400°C. This peak was attributed to the final melting of the bulk material, which was in agreement with Figure 14. The only events that appeared to reoccur during cooling are initial solidification, labelled as B, between 1380°C and 1330°C, and precipitation of the M_7C_3 carbide and final solidification, labelled as A, at 1240°C. This may indicate that the first three peaks that occur during heating were irreversible or otherwise attributed to non-equilibrium events and thus did not appear during cooling. As the stock powder was produced via water atomization, the phases

present within the powder were unlikely to be in an equilibrium state at ambient temperature prior to being scanned in the DSC and as such the peaks associated with their transformation or dissolution when heated would not have reappeared when cooled.

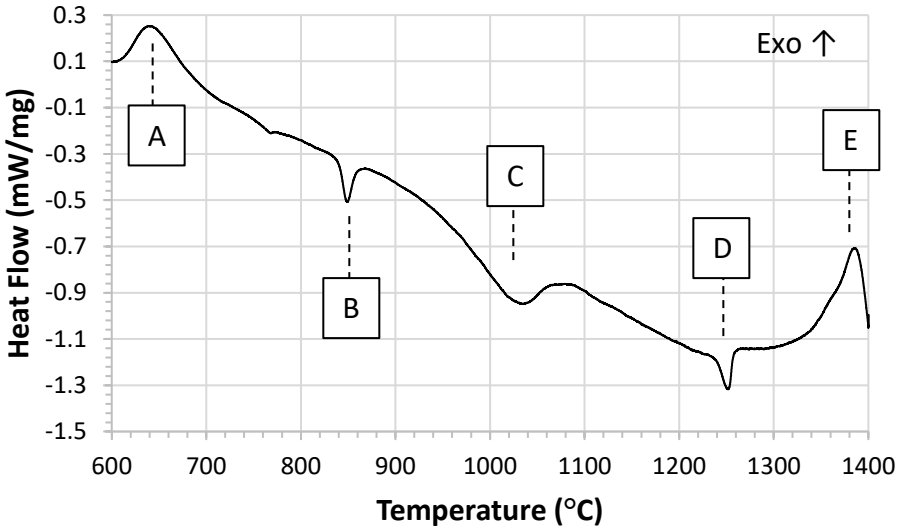

(a)

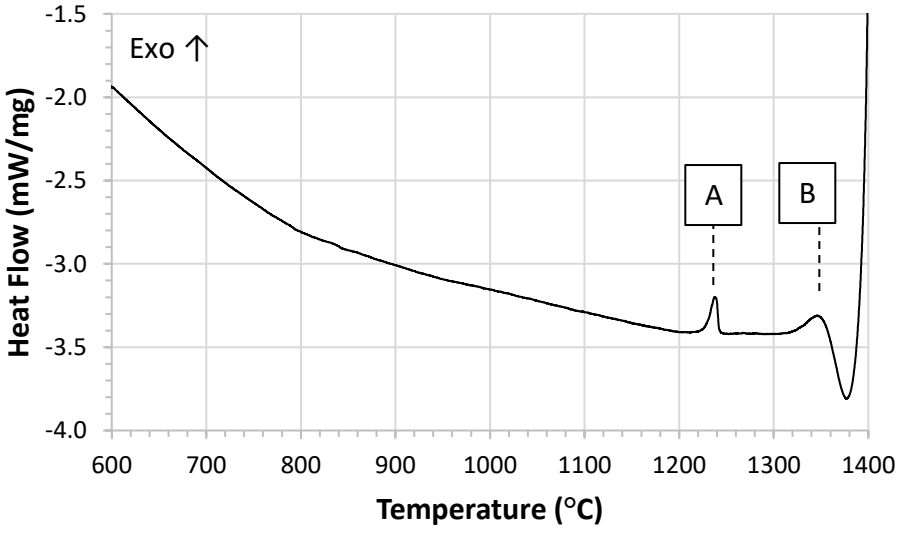

(b)

Figure 15 – DSC curves acquired from D2 powder samples heated to 1400°C. Data presented for (a) heating and (b) cooling.

The results of thermodynamic modelling and DSC inferred that liquid phase formation in the D2 should commence in the range of 1200 to 1240°C. Hence, to probe the LPS behaviour of the powder a series of thermal dilatometry experiments were completed wherein samples were isothermally held at 1000 to 1300°C. The results for select runs within the range of temperatures wherein a liquid phase was expected are shown in Figure 16. As would be expected, printed specimen experienced increased shrinkage with increased sintering temperature over this range. Higher temperatures would have invoked progressively greater volume fractions of liquid phase. The increased amount of liquid within the sample allows more pores to be filled fostering intense capillary action as well as increasing the overall material transport for further particle bond growth. This then invokes particle rearrangement and ultimately causes more shrinkage and higher sintered densities [20].

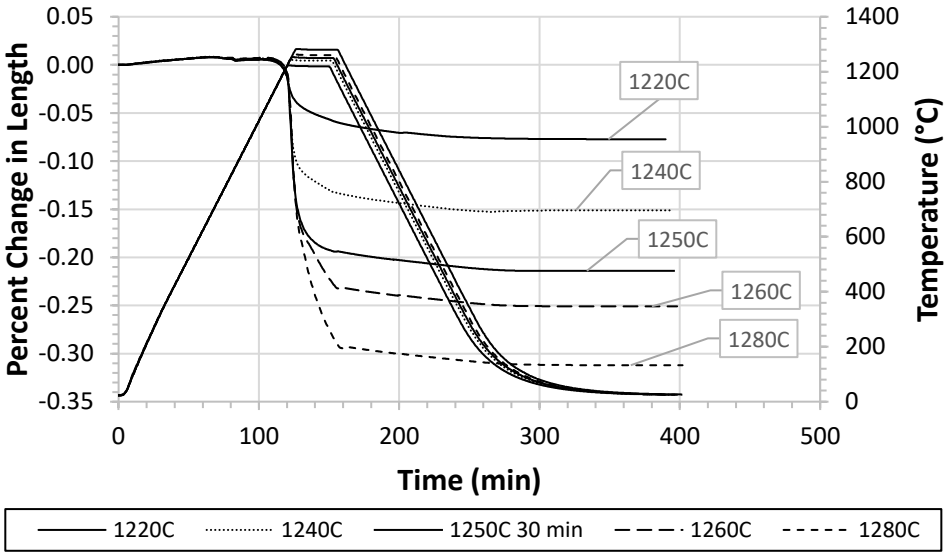

Figure 16 – Thermodilatometry results for D2 specimens sintered between 1220°C and 1280°C.

Table 4 shows the sintered densities of all dilatometer samples. These data indicated that, much like the measured shrinkage, part density increased with increased sintering temperature as well. However, the densities appeared to plateau at 1250°C, with all sinter

temperatures above it manifesting specimen of essentially the same final density. In addition, samples above 1260°C were noticeably distorted, with those sintered at 1280°C and 1300°C having suffered severe slumping. Figure 17 shows the extent of distortion resulting from sintering at 1300°C, wherein the sample had noticeably slumped due to gravity during sintering. These observations indicated that excessive liquid was present at temperatures of 1260°C and above, and provided an explanation for the apparent shrinkage shown in Figure 16 still occurring at these elevated temperatures despite no additional densification. These temperatures would be untenable for BJP processing as the complex printed geometry would most certainly be lost in the finished product.

Table 4 - Densities of samples sintered in the thermal dilatometer at various temperatures.

Sintering Temperature (°C)	Sintered Density (g/cm^3)	Percent of Full Theoretical Density
1000	4.18	53.6 %
1100	4.54	58.1 %
1200	4.40	56.4 %
1220	5.09	65.3 %
1240	7.07	93.1 %
1250	7.69	98.5 %
1260	7.70	98.7 %
1280	7.79	99.8 %
1300	7.59	97.3 %

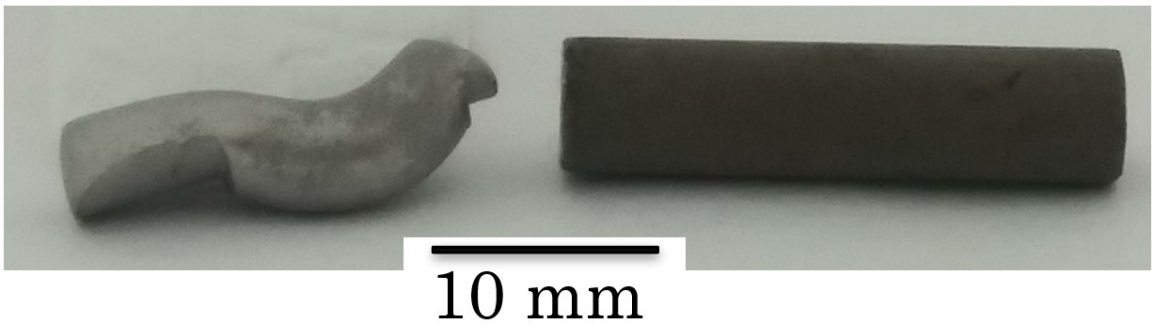

Figure 17 - Comparison between dilatometry samples sintered at 1300°C (left) and in the de-bound condition (right).

Figure 18 shows the microstructures of these samples sintered at the various temperatures. As one would expect, porosity (black feature) decreased with increasing sintering temperature. In this sense, 1220°C showed large amounts of porosity due to limited densification and while the 1260°C specimen showed only several small residual pores as it had reached near-full density. There was no significant reduction in porosity apparent but rather some noticeable grain coarsening in the samples sintered above 1250°C, and conversely there was no significant densification occurring below 1240°C. This indicated that the preferred sintering temperature was in the vicinity of 1240°C to 1250°C from the perspective of densification. Also of interest was the presence of an intergranular phase which appeared in the sample sintered at 1250°C and then more intensely, in that sintered at 1260°C. Visually similar phases were presented in ASM handbook 9 in which a sample of D2 was austenitized at 1230°C and air quenched [6]. Likewise, similar intergranular phases were observed in work by Hamidzadeh et al. and were attributed as alternating sequences of austenite and eutectic carbides [76].

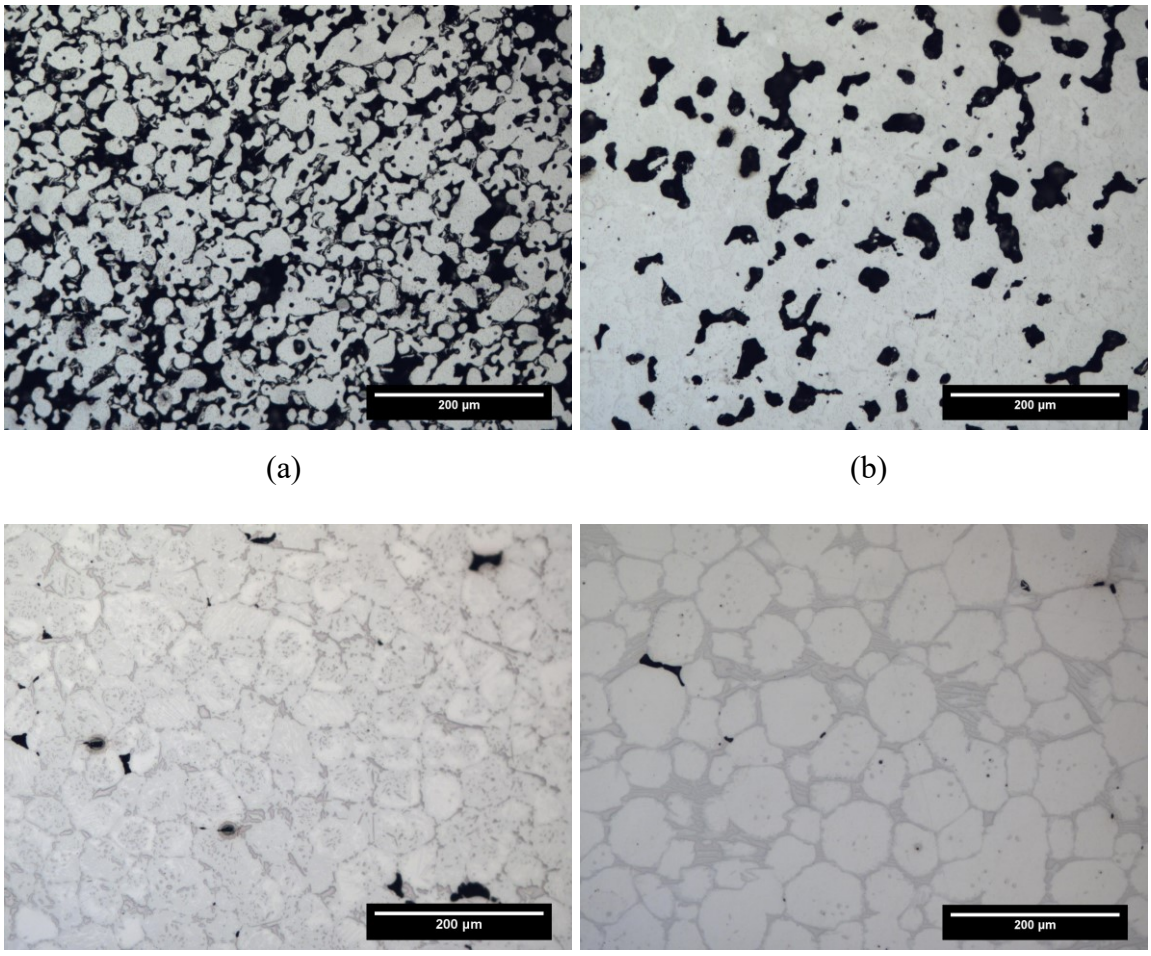

Figure 18 – Micrographs of the dilatometer sintered samples at 200x magnification, sintered at (a) 1220°C, (b) 1240°C, (c) 1250°C, and (d) 1260°C for 30 minutes.

The SEM images shown in Figure 19 allowed for further investigation into the microstructure of these samples. The only microstructure containing significant porosity within this set was the 1220°C specimen which, as discussed previously, demonstrated a clear lack of densification. As well, the grain coarsening shown at higher temperatures in Figure 18 can also be seen in these images as well as the intergranular eutectic structure observed with the higher temperatures. The composition of the latter was assessed using energy dispersive spectroscopy (EDS) mapping. The results (Figure 20) agreed with prior studies in that the eutectic feature was comprised of alternating regions with one enriched in iron and the second in vanadium, chromium, and carbon. These suggested

that these were alternating phases of austenite and chromium/vanadium carbide consistent with Hamidzadeh et al [76]. Based on existing literature of the carbides typically present in D2, primary M_7C_3 (M = Fe, Cr, V) carbides form along grain boundaries [41]. Hence, the intergranular carbide phase was likely of the M_7C_3 character.

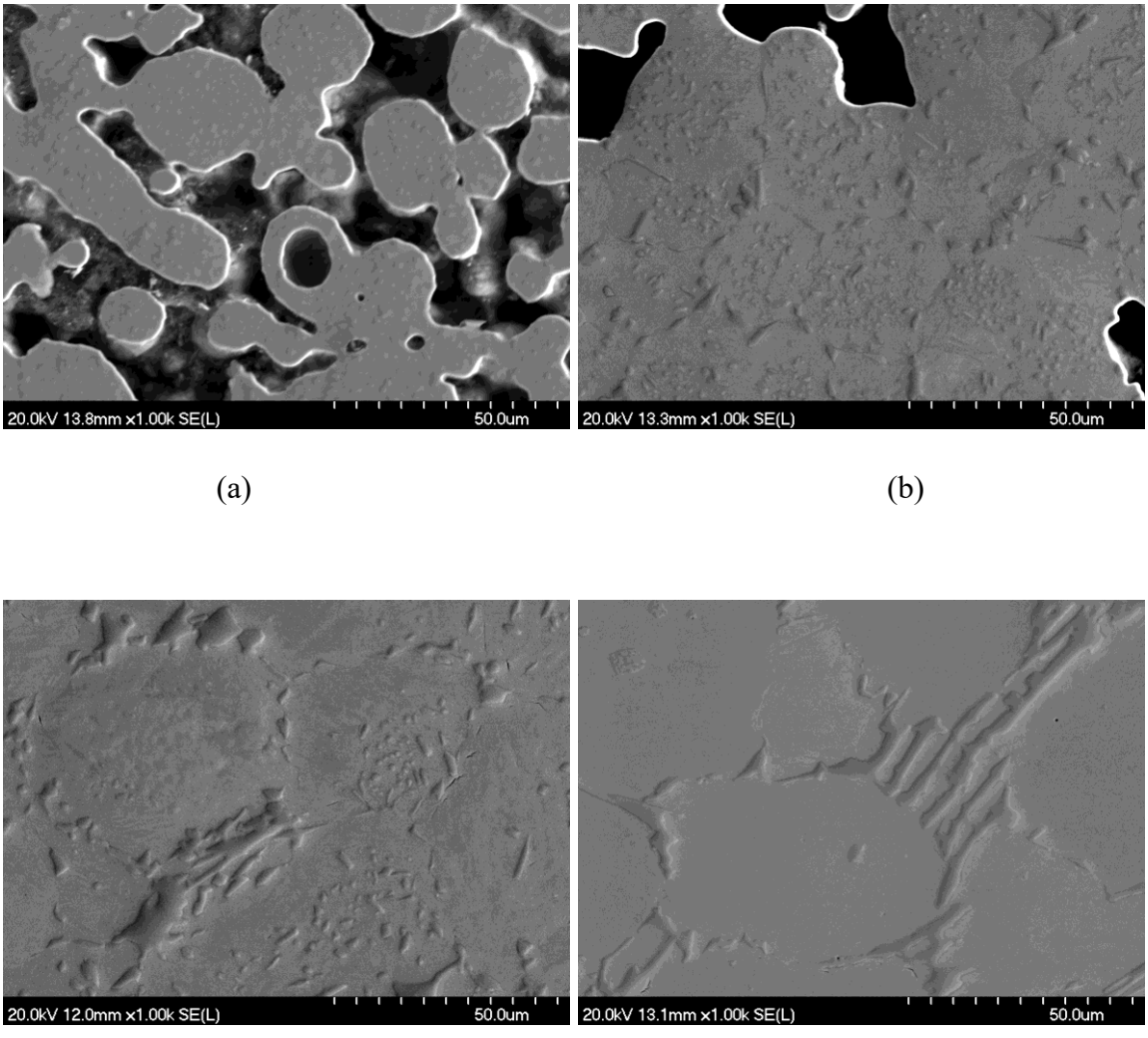

Figure 19 – Microstructures in dilatometer sintered samples sintered at (a) 1220°C, (b) 1240°C, (c) 1250°C, and (d) 1260°C as observed with a SEM.

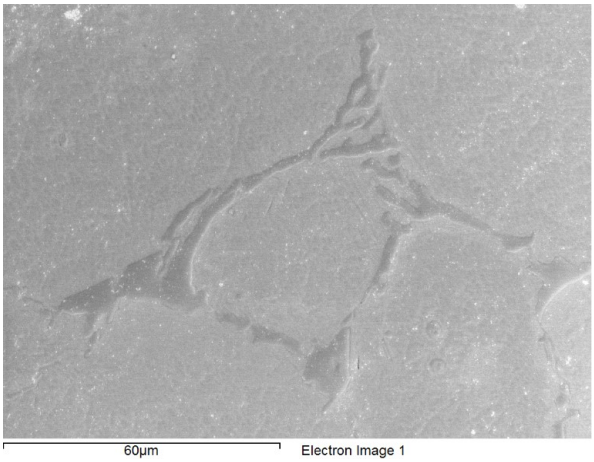

(a)

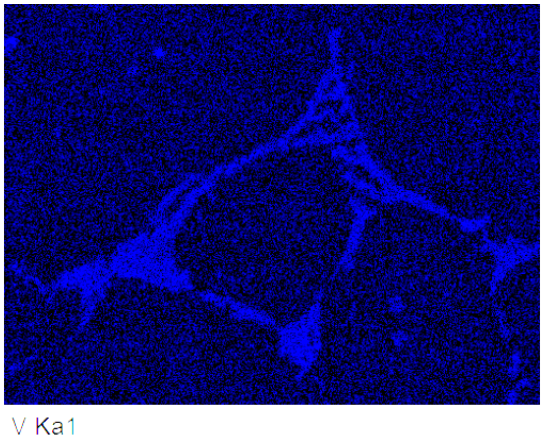

(b)

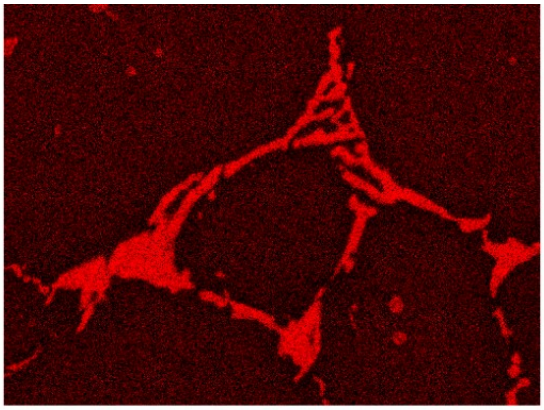

(c)

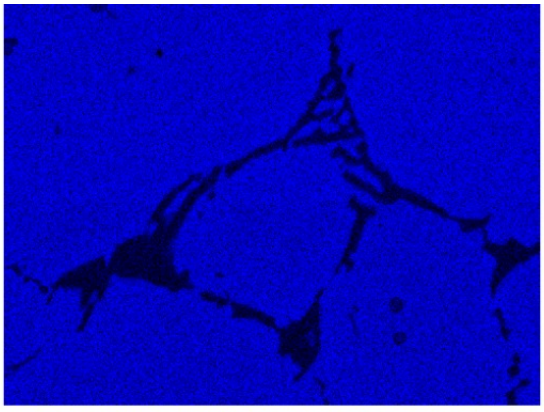

(d)

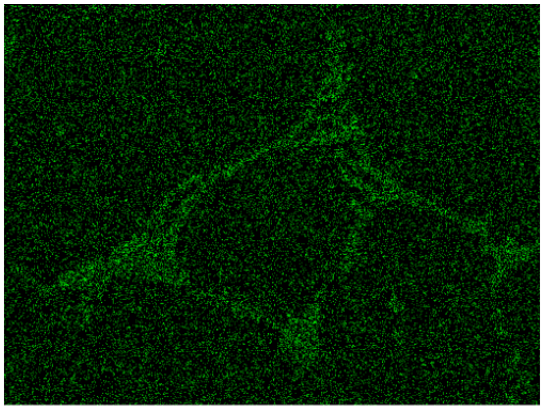

(e)

Figure 20 – EDS mapping results for a dilatometer sample sintered at 1260°C showing (a) the original SEM image, as well as elemental maps for (b) vanadium, (c) chromium, (d) iron, and (e) carbon.

Thermodilatometry tests were also performed at a constant temperature with varied isothermal holds to examine the effect of sintering time. Figure 21 shows the curves for samples sintered at 1250°C for times ranging from 10 to 90 minutes. As expected, shrinkage increased with increasing hold time as this allowed more time for diffusion to occur. However, there was a point of diminishing returns as the difference in final shrinkage between the 60-minute and 90-minute sinters was negligible. The presence of this plateau and lack of noticeable distortion directly contrasts the lack of plateau due to significant slumping distortion which was seen in the previous thermodilatometry sinters shown in Figure 16 and Figure 17. Since the principal driving force behind sintering is the reduction in surface free energy and pore boundary surface area, an increase in sintering time would cause pores to continue to shrink or be eliminated until an equilibrium is achieved between the gas pressure within the pores and the surface energy of the pore boundaries [78]. At this point of equilibrium, further increases to the hold time have no effect on any remaining pores and densification is halted.

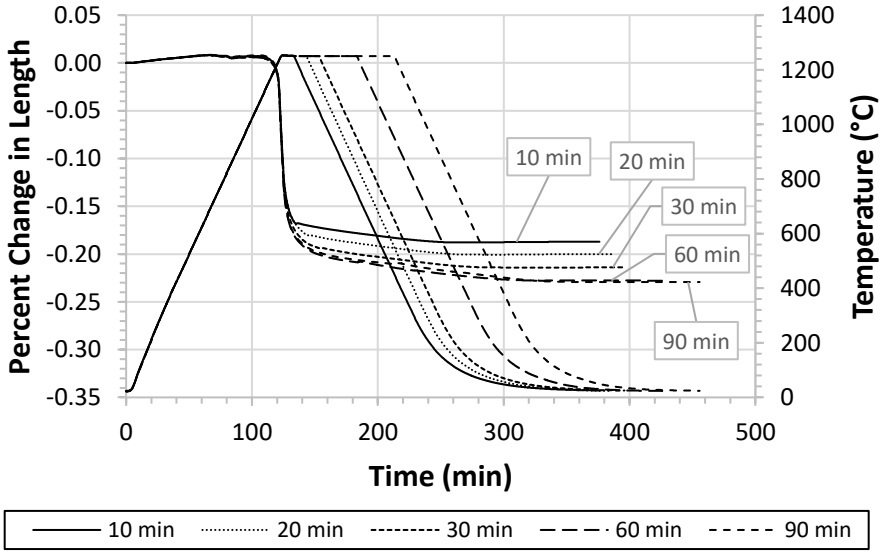

Figure 21 – Thermodilatometry curves for printed D2 specimen held at 1250°C for various periods.

The microstructures of samples sintered at various hold times are shown in Figure 22 and Figure 23. These images showed decreasing amounts of porosity with longer hold times, though this was only true for the 10- and 30-minute holds. The 60- and 90-minute holds showed no additional reduction in porosity and, similar to the varied sinter temperature microstructures, showed noticeable coarsening of the grains and intergranular carbides; the latter was now predominantly present as large blocky features with a clear reduction in the amount present in a eutectic format.

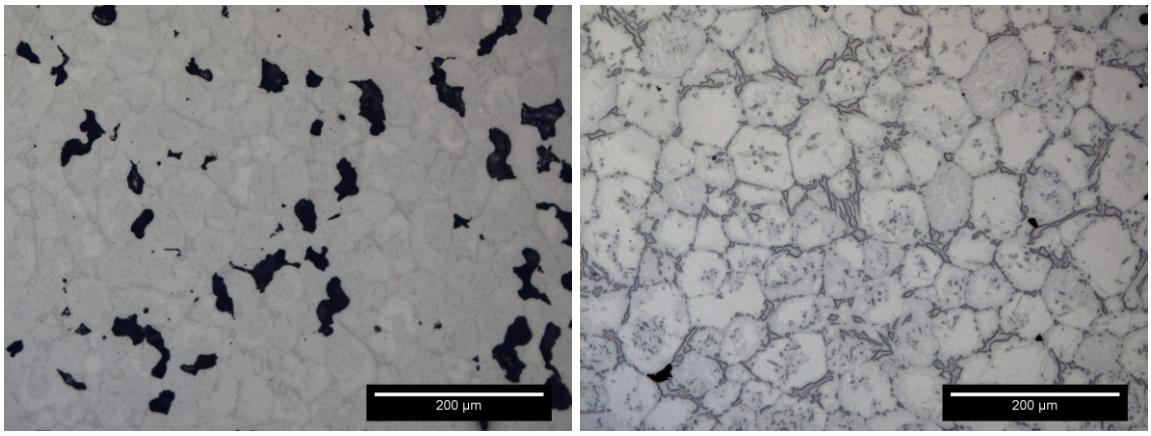

(a) (b)

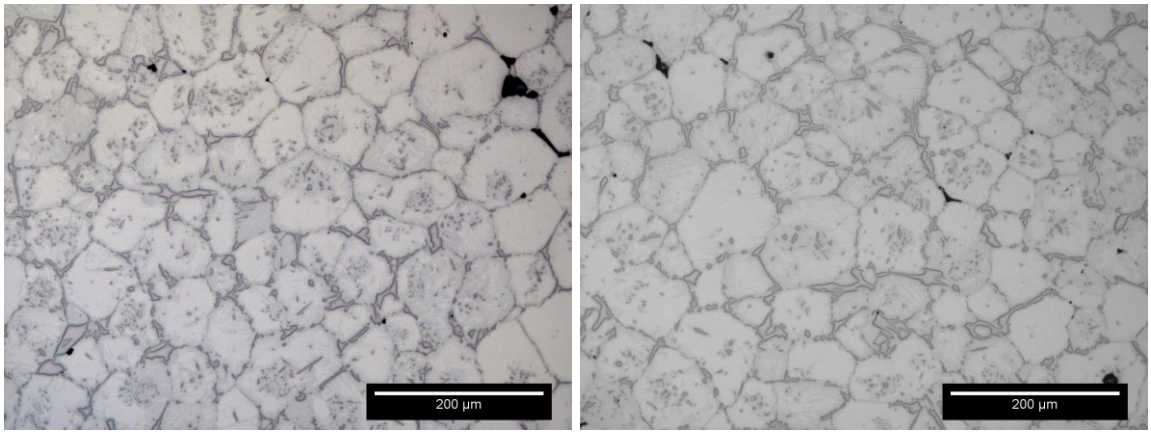

(c) (d)

Figure 22 – Micrographs of the dilatometer sintered samples at 200x magnification, sintered at 1250°C for (a) 10 minutes, (b) 30 minutes, (c) 60 minutes, and (d) 90 minutes.

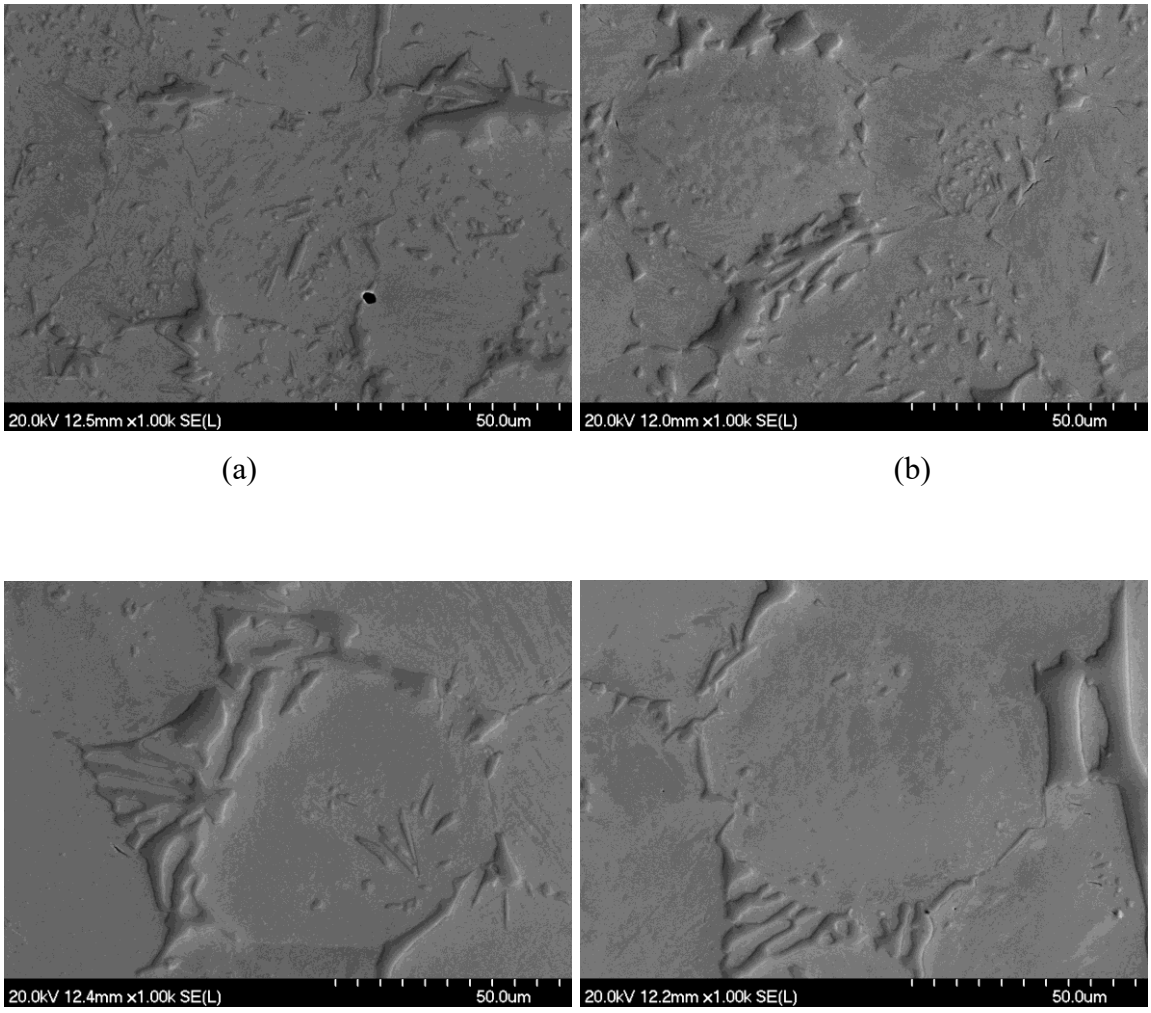

Figure 23 - SEM images of the dilatometer sintered samples, held at 1250°C for (a) 10, (b) 30, (c) 60, and (d) 90 minutes.

3.4.1.3 Bulk Sintering

Figure 24 shows a comparison of the achieved densities in thermodilatometry cylinders versus the larger TRS bars as a function of sintering temperature. As discussed above, due to the smaller nature of the cylinders, their measured densities included a small degree of inaccuracy, but were largely similar to those of the TRS bars. Based on the data

shown here, optimal sintering temperature again ranged between 1250°C (98.9% theoretical density) and 1260°C (98.6% theoretical density).

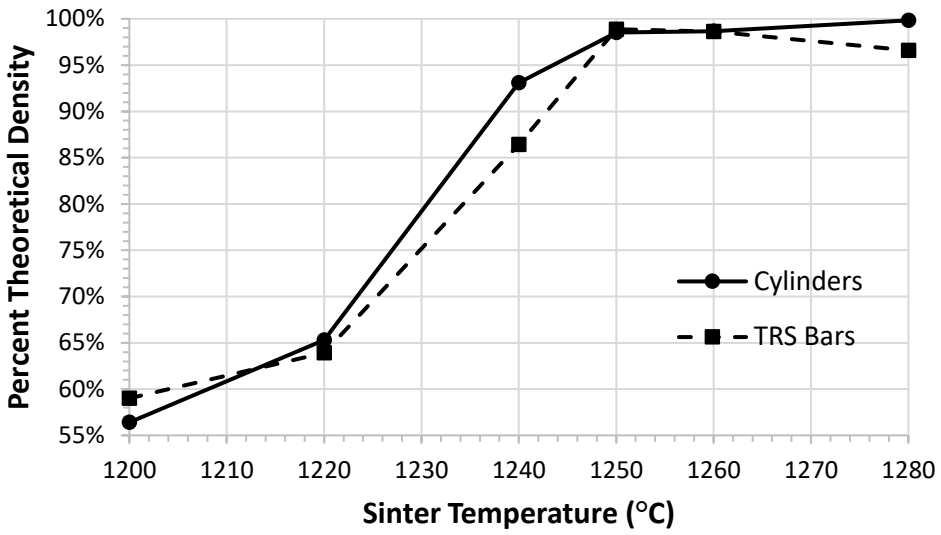

Figure 24 – Comparison of sintered densities for binder jet printed dilatometry cylinders and TRS bars as a function of sintering temperature. All samples sintered at temperature for 30 minutes under a high vacuum atmosphere.

Microstructures of the batch sintered TRS bars are presented in Figure 25 below. These images show a highly similar transition in densification with increased sintering temperature to the equivalent micrographs taken for the dilatometer-sintered counterparts. TRS samples sintered at 1220°C remained highly porous with limited inter-particle bonding and minimal pore coalescence and/or elimination. Sintering at 1240°C invoked more intensive inter-particle bonding, a reduction in the amount of porosity present, and gains in density. Specimen sintered at 1250°C and 1260°C maintained comparable microstructures. Both demonstrated significant improvements in density with only sporadic pores remaining and all particles now interconnected. The alternating austenite and eutectic carbide phases observed in the dilatometer-sintered samples were also present along many grain boundaries in these sintered TRS samples.

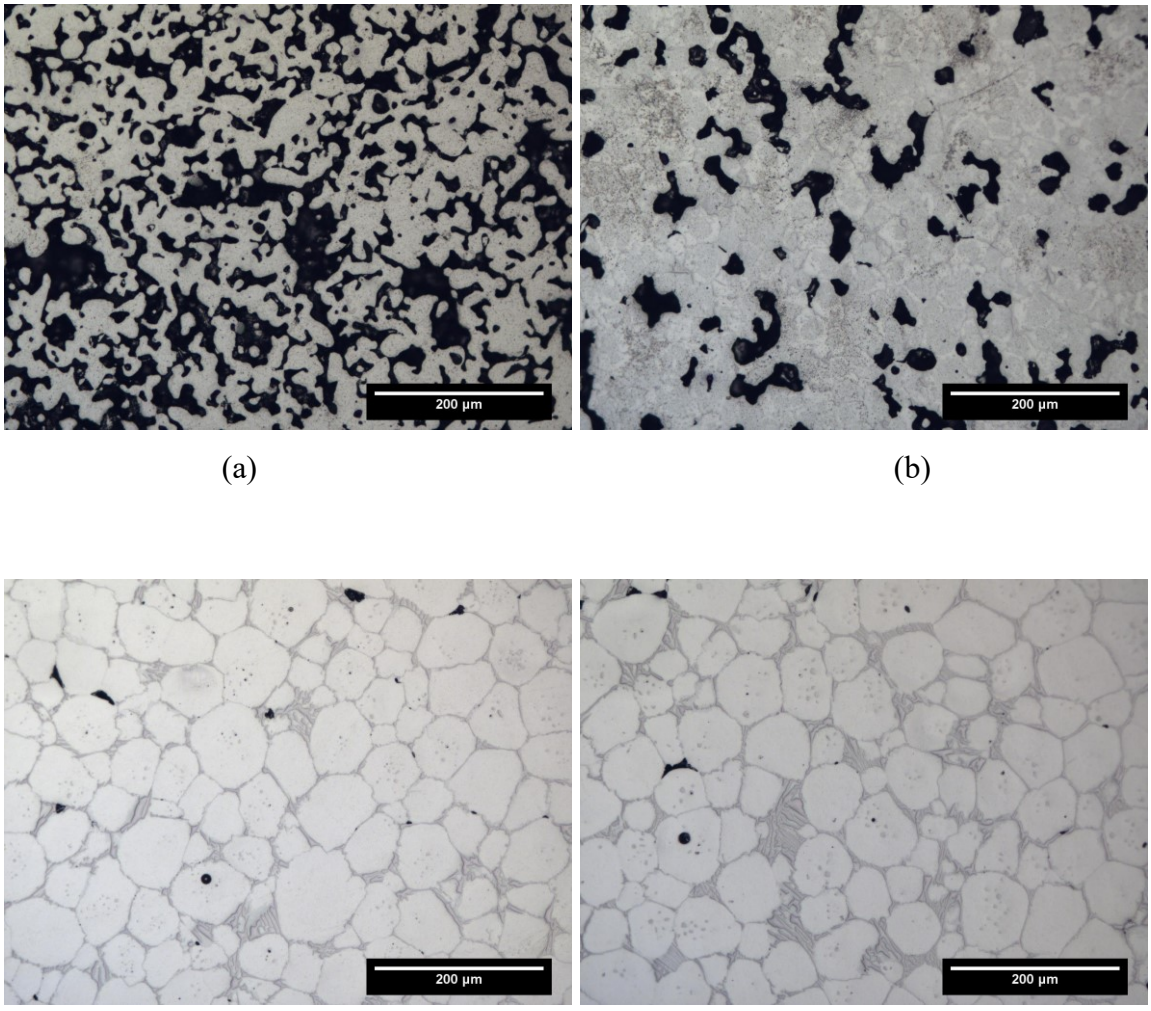

(a) (b)

(c) (d)

Figure 25 – Micrographs of TRS samples sintered at (a) 1220°C, (b) 1240°C, (c) 1250°C, and (d) 1260°C for 30 minutes under high vacuum.

The microstructures of the sintered TRS bars are expanded upon in the SEM images presented in Figure 26. These images show the noticeable coarsening of grains from 1240°C to 1260°C, as well as the presence of the alternating carbide and prior austenite phases in the 1250°C and 1260°C samples as was seen in previous micrographs.

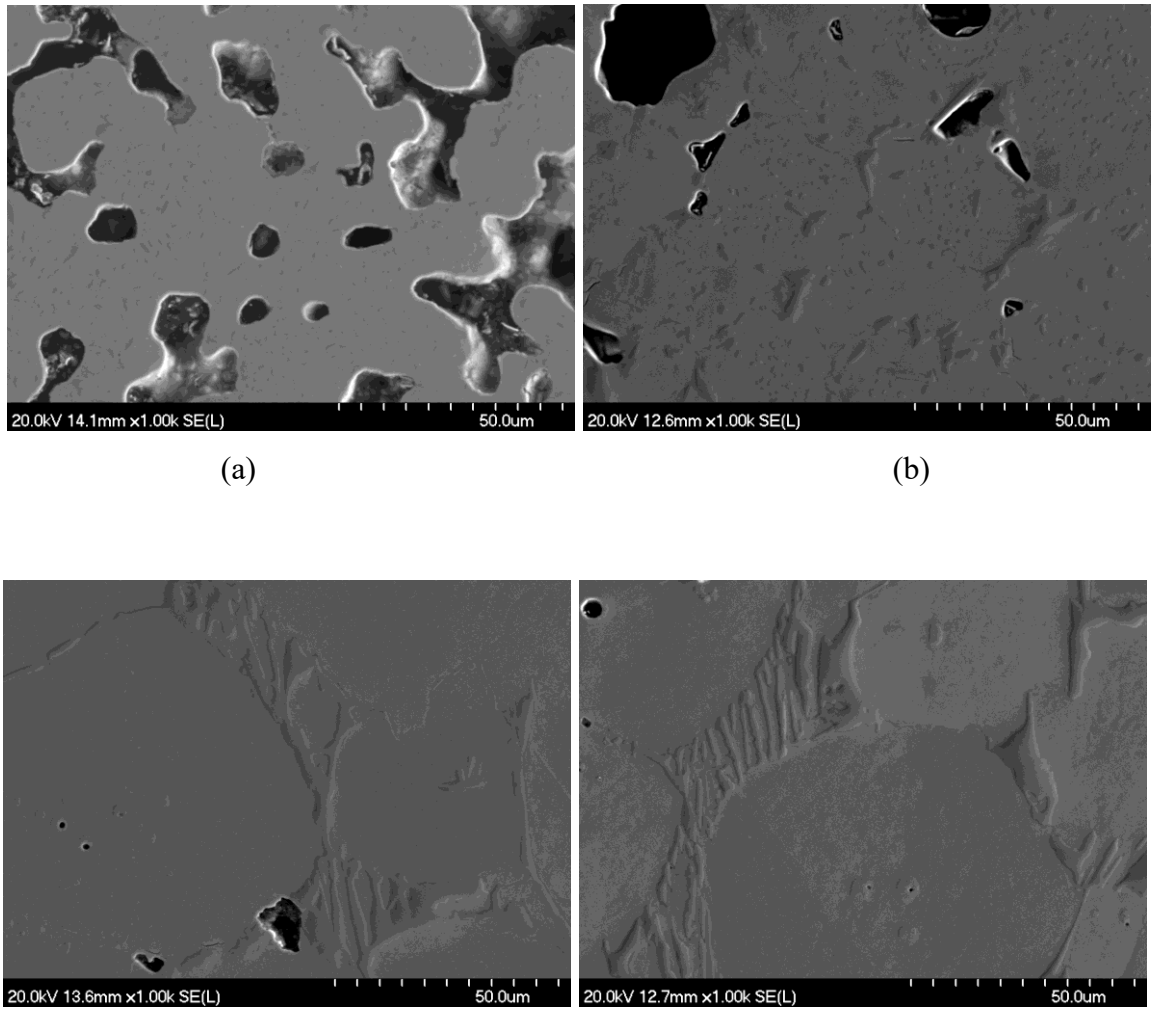

Figure 26 - SEM images of the batch sintered TRS samples, sintered at (a) 1220°C, (b) 1240°C, (c) 1250°C, and (d) 1260°C for 30 minutes.

3.4.2 Comparison to Wrought D2

To determine the potential industrial utility of the BJP process, it is insightful to understand how BJP products compare to a conventional wrought D2 counterpart. As such, wrought D2 was acquired in an annealed form and compared to the BJP + sinter products through several means. The first of which centered on a comparison of microstructural transitions as assessed through DSC. Traces acquired from an as-sintered BJP product and annealed wrought D2 are shown in Figure 27. Three peaks were evident in the former including a large exothermic peak at 725°C (A) and two endothermic events

at 770°C and 840°C. Peak A was absent from the trace of the annealed wrought D2, although peaks B and C prevailed and were more acute.

As discussed in Figure 15, the exothermic peak which began at approximately 620°C was attributed to the transformation of martensite to austenite, though in Figure 27 this peak appeared to span a much larger temperature range before reaching a maximum at 725°C, nearly 80°C higher than that shown in Figure 15. Furthermore, this peak is absent from the trace for the annealed wrought D2 sample, which is likely indicative of a total absence of martensite in the sample due to annealing. Peak B appeared in both traces, though seemingly slightly truncated in the as-sintered BJP trace likely due to overlap with peak A, and was attributed to the partial transformation of the M_7C_3 carbide to $M_{23}C_6$, in contrast to the findings of Bombac et al. wherein it was attributed to the reverse transformation of $M_{23}C_6$ carbide to M_7C_3 [74]. The basis for this claim is due to work done by Kondrat'ev et al., where the transition of $23M_7C_3 \rightarrow 7M_{23}C_6 + 27C$ was observed and determined experimentally while holding at elevated temperature for several hours [79]. This same transition was also reported by several other authors also examining the carbide behaviour of steels {Formatting Citation}. It is also believed that the carbon released during this transition then contributed to the transformation of the relatively carbon-poor ferrite phase to carbon-rich austenite, shown as peak C in Figure 27. This would also account for the notable decrease in the amount of M_7C_3 carbide during the ferrite to austenite transformation as shown in Figure 14 as well as the subsequent slight increase in $M_{23}C_6$ content. As mentioned briefly, the final thermal event appearing in these traces, peak C, was endothermic in nature and occurred at approximately the same temperature for both samples, though the height of this peak saw large variation between the two traces. This event, as discussed previously in Figure 15, was attributed to the ferrite to austenite transformation and is in agreement with the work of Bombac et al. [74].

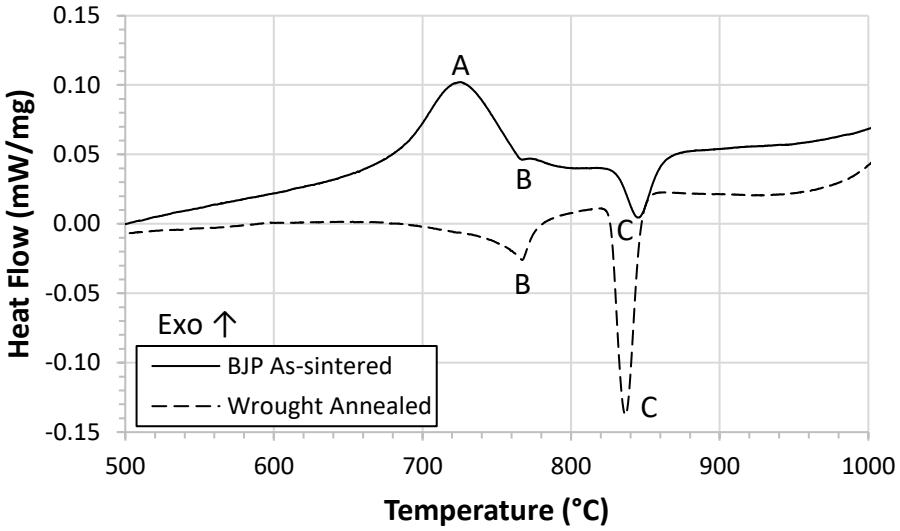

Figure 27 – DSC traces for wrought and BJP D2 samples in the annealed and as-sintered (1250°C for 30 minutes) conditions respectively.

Prior to deployment in an end-use application, D2 is typically heat treated to maximize hardness and strength. As such, the effects of heat treatment were also considered for the BJP and wrought materials. Here, samples were heat treated through a sequence of austenitization at 1010°C for 15 minutes, air cooling to ambient, and then tempering at 204°C for 2h; the standard process for D2 as defined in ASTM A681 – 08 [3]. DSC traces acquired from each material are shown in Figure 28.

As was observed in Figure 27, three thermal events were apparent between 500°C and 1000°C in the heat-treated samples as well. Of notable difference, however, is that peak A occurred at a lower temperature in the heat-treated samples (approximately 660°C) than the as-printed BJP sample, which matches more closely with peak A in Figure 15. Furthermore, this peak saw a much larger amount of energy released in the as-sintered sample compared to those which were heat-treated. Due to relatively rapid cooling rates following sintering, it is likely that a surplus of martensite formed in the as-sintered BJP sample, resulting in more amounts of austenite being formed on re-heating in the DSC when compared to the heat-treated samples. Similarly, the apparent shift in peak temperature may instead be interpreted as this transformation being drawn out over a longer time period in the as-sintered sample due to the larger quantity of martensite

transforming to austenite. Peak B, again being attributed to the transformation of M_7C_3 carbide to $M_{23}C_6$, occurred at 770°C in strong agreement to the same peak in Figure 27. Interestingly, the only significant difference between the traces of the two heat-treated samples was the temperature and height of peak C, previously attributed to the ferrite to austenite transformation. As both samples underwent the same thermal profile during heat-treatment, these differences in height and temperature of occurrence are likely due to the slightly different chemistries shown in Table 3. Aside from the slight peak C shift, both heat-treated traces line up nearly perfectly, particularly in comparison to the two traces presented in Figure 27 which were highly different with one another. This would appear to indicate that the heat-treatment process affected both the wrought and BJP samples similarly in terms of resulting phase composition.

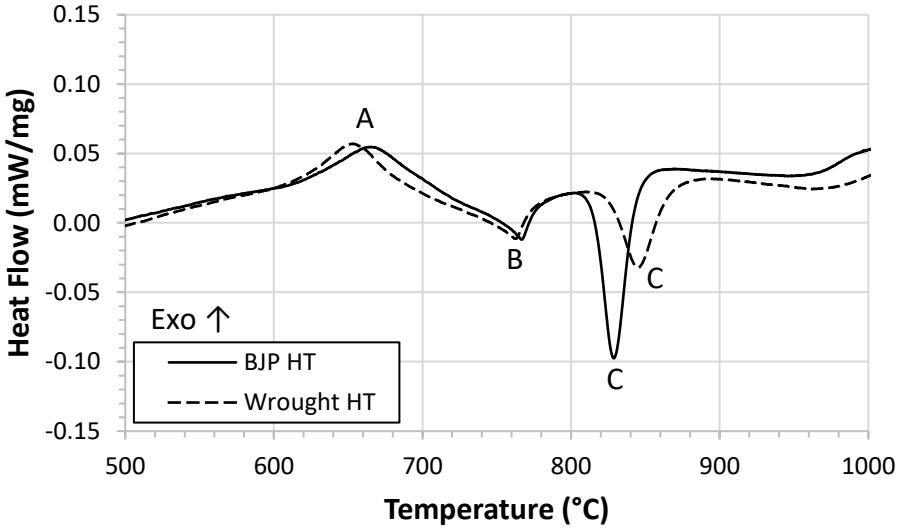

Figure 28 - DSC traces acquired from wrought and BJP D2 samples after heat treatment. BJP sample sintered at 1250°C for 30 minutes.

The general microstructures observed in heat treated specimen are shown in Figure 29 with composition maps shown in Figure 30 and Figure 31. Overall, a distinct difference in the relative homogeneity of carbide distribution was observed. Within the BJP product, carbides were present as relatively coarse intergranular features and as clusters of smaller

particles within grains. This distribution was modestly more favourable than that observed in the as-sintered product (Figure 20) wherein carbides were present as an effectively continuous intergranular feature and largely absent from the grains themselves. This indicated that a portion of the carbides present after sintering had dissolved and re-precipitated to manifest a marginally more homogenous distribution. Comparatively, the wrought sample exhibited a more refined and homogenous distribution of smaller carbides throughout the ferrous matrix. Interestingly, the carbide distribution present in BJP products sintered at 1240°C (Figure 19(a)) was much closer to the wrought system in terms of the nominal size and homogeneity of carbide distribution. However, this sintering temperature manifested an inferior quality sample from the perspective of sintered density (Table 4). This highlighted the interdependency of density and carbide distribution on sintering temperature and how a balance between these factors needs to be considered in the context of BJP of D2 tool steel.

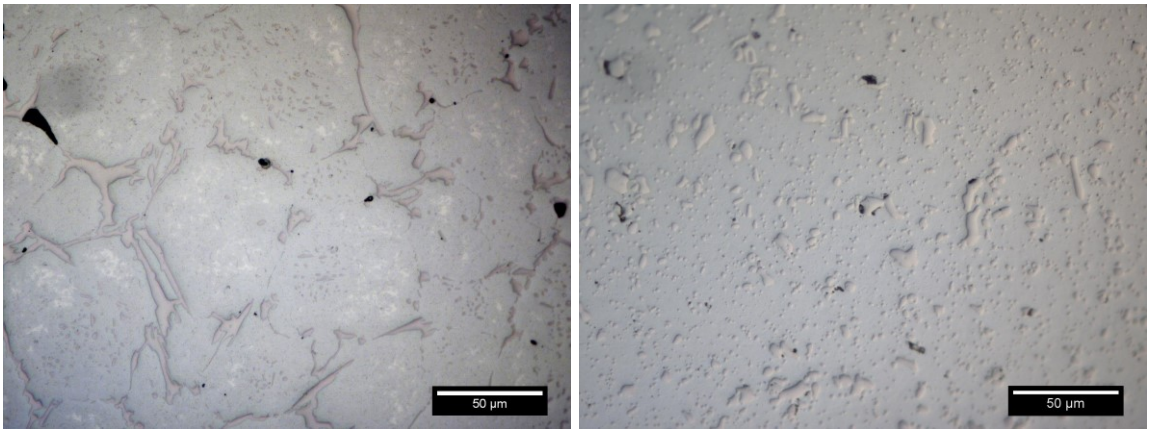

(a) (b)

Figure 29 – Microstructures of (a) BJP and (b) wrought D2 specimen after heat treatment. BJP sample originally sintered at 1250°C for 30 minutes.

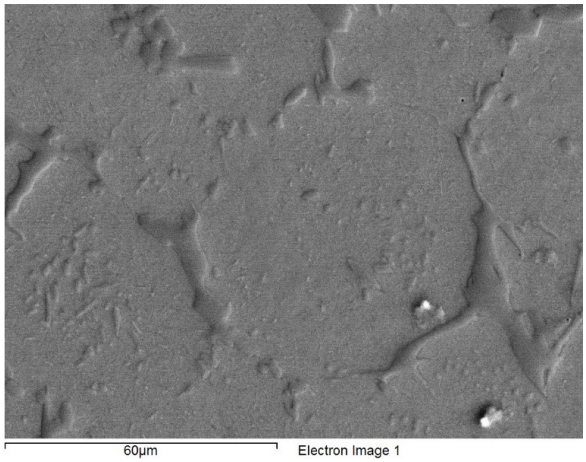

(a)

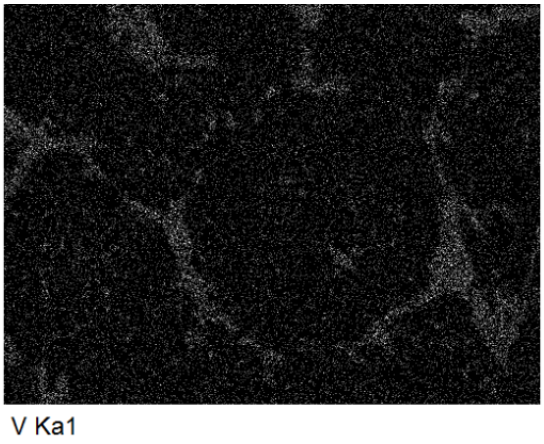

(b)

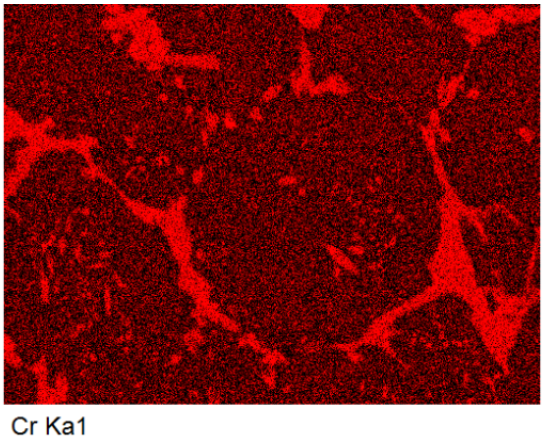

(c)

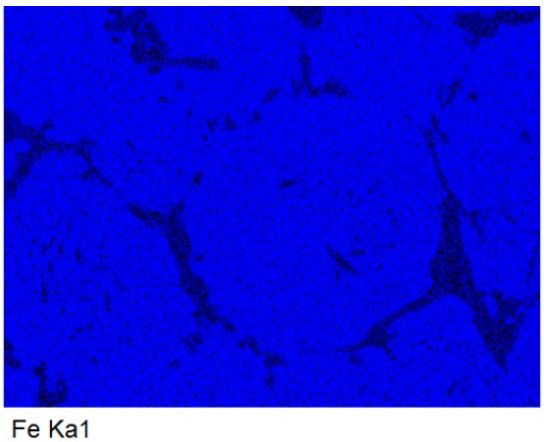

(d)

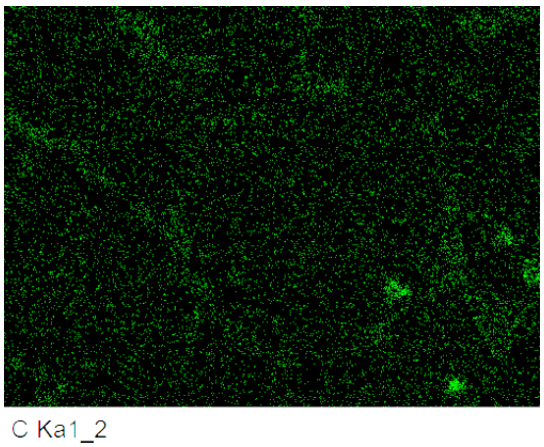

(e)

Figure 30 – EDS mapping of a heat-treated BJP D2 sample, showing (a) the original SEM image, as well as the spatial distributions of (b) vanadium, (c) chromium, (d) iron, and (e) carbon. BJP sample originally sintered at 1250°C for 30 minutes.

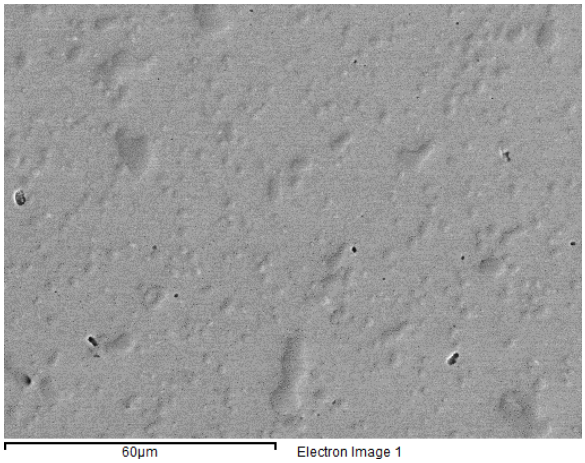

(a)

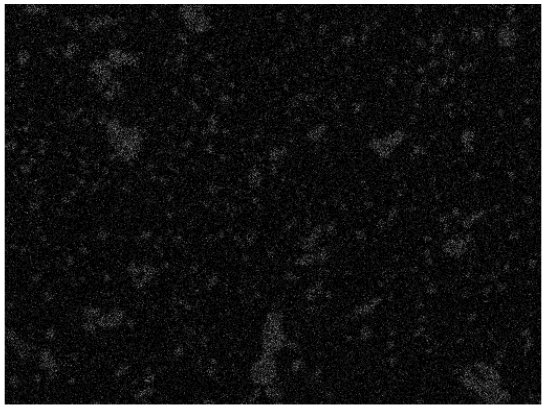

V Ka1

(b)

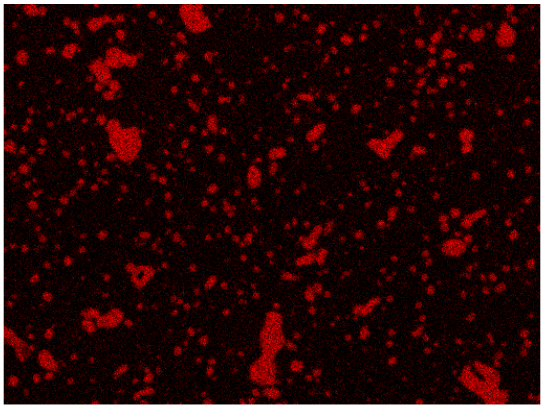

Cr Ka1

(c)

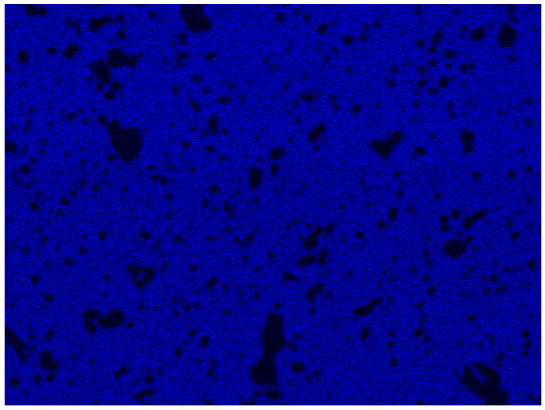

) Fe Ka1

(d)

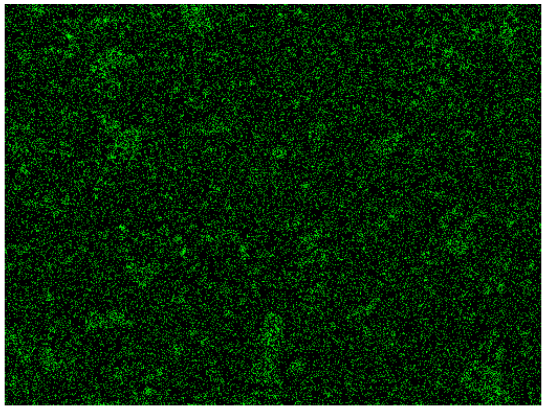

C Ka1_2

(e)

Figure 31 – EDS mapping of a heat-treated wrought D2 sample, showing (a) the original SEM image, as well as the spatial distributions of (b) vanadium, (c) chromium, (d) iron, and (e) carbon.

Hardness data for printed and wrought samples in the heat treated and as-sintered/annealed states are shown in Table 5. Each sample was tested a minimum of 3 times to establish an average value and standard deviations. Per ASTM A681-08, the minimum hardness required for heat treated D2 is 59 HRC [3]. As such, the wrought product was compliant while the BJP material was slightly below spec, although the value was within the range of standard deviation. The carbide phases and the size/homogeneity thereof have a major influence on material hardness [1, 84]. As wrought D2 was superior in this context, the heightened hardness was to be expected. As-sintered BJP and annealed wrought materials were significantly softer as neither was processed through the appropriate heat treatment sequence necessary to achieve peak hardness.

Table 5 - The measured hardness values for as-sintered, as-received, and heat-treated binder jet printed and wrought D2 samples.

	Sample Condition	Average Hardness, HRC
Binder Jet Printed	As-sintered	38 ± 2
	Heat treated	57 ± 2
Wrought	As-received (annealed)	24
	Heat treated	61 ± 1

The final means of comparing heat treated BJP/wrought specimen was compression testing. Examples of the resultant stress-strain curves attained are presented in Figure 32 and summarized in Table 6. The tabulated data is the averaged result of two samples per sample condition with the calculated standard deviations shown alongside. In all instances, samples were loaded through yielding and only to a point of plastic deformation whereby the offset yield strength could be determined. Although the performance of each material was comparable, that of the wrought form was modestly superior. In this sense, the difference in elastic modulus was only 1 GPa (<1%) while that in yield strength was 214 MPa (~12%). These differences, like those in hardness, were also ascribed to the known dissimilarities in carbide distributions.

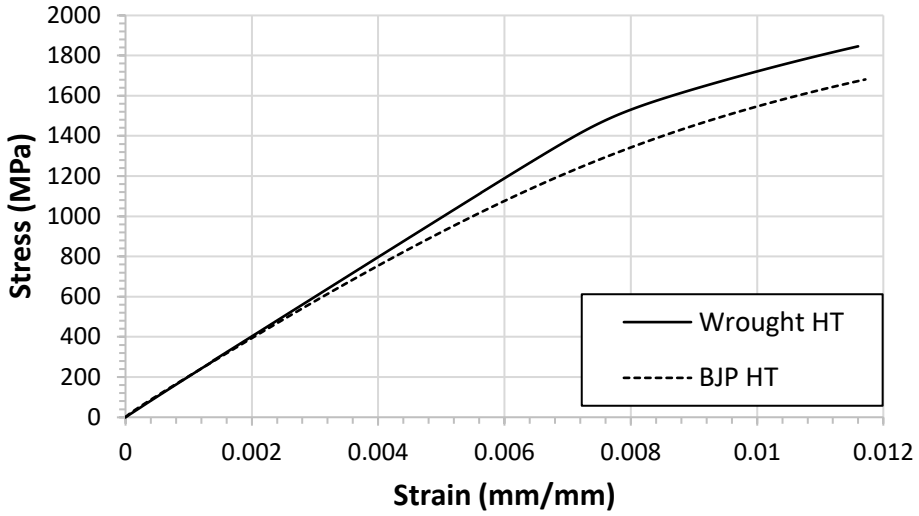

Figure 32 – Compressive engineering stress-strain curves for heat treated D2 specimens processed through wrought forming and BJP.

Table 6 – Summary of compressive properties measured for wrought and BJP materials in a heat treated state.

Sample	Elastic Modulus (GPa)	0.2% Offset Yield Stress (MPa)
Wrought HT	192 ± 7	1747 ± 104
BJP HT	191 ± 1	1533 ± 53

3.5 Conclusions

In this work, water atomized D2 tool steel powder was successfully processed through all the steps of BJP as well as typical heat-treatment procedures for the alloy. The resulting microstructure and select mechanical properties were then compared to a wrought counterpart. Based on the results obtained, the following conclusions have been reached:

1. Peak densification of the D2 powder mandated was only achieved with liquid phase sintering. This produced a high-density product but also manifested coarsening and segregation of carbide phases in the finished product.
2. Effective sintering conditions for BJP D2 tool steel were determined to be 1250°C for 30 minutes. Sintering for the same time at 1260°C or higher resulted in

distortion whereas at 1240°C and below the sintered product part exhibited significant amounts of residual porosity.

3. BJP products were responsive to the heat treatment practice commonly applied to wrought D2. This improved hardness significantly but had limited impact on the carbide distribution present after sintering.
4. Heat treated samples of wrought D2 were moderately higher in hardness, elastic modulus, and offset yield strength as compared to BJP counterparts although the differences in all regards were relatively minor. These advantages were ascribed to a more refined and homogenous distribution of carbide phases in the wrought system.

3.6 Acknowledgements

The authors would like to thank the Natural Sciences and Engineering Research Council of Canada (NSERC) Holistic Innovation in Additive Manufacturing (HI-AM) Network for funding for this research and GKN Sinter Metals for providing the stock water atomized D2 powder used in this work. Additional thanks to Mr. Randy Cooke and Dr. Addison Rayner for their technical and laboratory assistance, as well as Mr. Albert Murphy and Mr. Mark MacDonald for machining samples.

CHAPTER 4 – SUMMARY AND CONCLUSIONS

The research presented here demonstrates the analysis and optimization of key processing parameters throughout the binder jet printing and post-printing process of a water atomized D2 tool steel powder. Through careful management of post-printing heating cycles, the resulting printed parts were tailored to achieve near full density (98.9% theoretical density) without noticeable physical distortion and with highly similar mechanical properties to the wrought counterpart.

The preliminary stages of this research surrounded the determination of ideal sintering conditions through DSC scans as well as several dilatometry tests at various sintering temperatures and hold times. The DSC results confirmed with both literature and FactSage-produced simulations the temperatures at which key thermodynamic events occurred upon heating the given material composition. These thermodynamic events corresponded to material transitions such as dissolution of the two primary carbides present within the alloy ($M_{23}C_6$ and M_7C_3) as well as the onset of liquid formation within the microstructure. With the apparent onset of liquid formation beginning at approximately 1200°C and continuing to melt until fully liquified by 1380°C, the ideal sintering window was initially set as being between 1200°C and 1300°C to avoid significant distortion due to excessive liquid formation.

To confirm these expectations and to further narrow the ideal sintering window, thermodilatometry tests were run to examine the sintering behaviour of individual samples held at temperatures within this initial range for 10 – 90 minutes. These tests produced samples with densities up to 99.8% theoretical density and with increasing degrees of distortion with higher temperatures. The resulting thermodilatometry shrinkage curves, shown in Figure 16 and Figure 21 for constant hold time and constant sinter temperature respectively, demonstrated a notable difference between the two data sets. For a constant hold time, increasing the sintering temperature produced increasingly shorter samples with no apparent diminishing returns in terms of final sample length, whereas the samples sintered at a constant temperature for various hold times similarly produced increasingly shorter samples with longer hold times, but instead showed minimal changes between final sample length at longer hold times. In other words, in the

ranges examined, a plateau was reached in terms of sample shrinkage for the constant temperature samples but was not apparent in those with a constant hold time. Nonetheless, the density and microstructural data helped narrow the sintering window to between 1240°C and 1260°C for a hold time of 30 minutes to achieve high densities while avoiding distortion and unnecessary grain coarsening in samples.

Due to the small nature of the thermodilatometry samples, density measurements were found to have a degree of variability within individual samples and were deemed to be likely somewhat inaccurate as a result. To follow up on these data inconsistencies, larger TRS bars were printed and processed in the same manner as the thermodilatometry samples to verify the final sintered densities for the given sintering window. The TRS bars showed highly similar measured densities to those of the thermodilatometry samples, confirming that the ideal sintering window was indeed in the range of 1250°C to 1260°C for a hold time of 30 minutes. Given that the densities produced by sintering at these temperatures were virtually the same (98.9% versus 98.6% theoretical density respectively) and that there was noticeable grain coarsening occurring at sinter temperatures above 1250°C, the ideal sintering conditions were determined to be 1250°C for 30 minutes.

For BJP produced parts to be industrially or commercially viable, they must demonstrate similar mechanical properties to their existing wrought counterpart. Hence, wrought D2 tool steel was sourced, and both wrought and BJP samples were subjected to heat treatment procedures typical for D2 tool steel. To determine the effectiveness of the heat treatment process in the BJP samples compared to that of the wrought, heat-treated samples of both were examined in DSC to examine the similarities and differences between thermodynamic events occurring during reheating. It was found that both wrought and BJP samples showed highly similar DSC scans post heat treatment, indicating that the procedure had a similar effectiveness on both samples. To further investigate this comparison, the microstructures and several key mechanical properties of both the wrought and BJP heat-treated samples were examined. Microstructural analysis revealed relatively coarse intergranular carbides and smaller clusters of carbides within grains of the heat-treated BJP sample, whereas the heat-treated wrought sample appeared

to have a much more refined and homogeneous distribution of finer carbides. These microstructural differences resulted in slightly elevated hardness and offset yield strength values for the wrought samples but produced no difference in elastic modulus between the two sample types.

In conclusion, this work has proven that a water atomized D2 tool steel powder can be processed through BJP to produce near full density parts with minimal distortion. Furthermore, via post-printing heat-treatment, these printed parts can achieve hardness and compressive properties of a similar caliber to that of the wrought counterpart.

4.1 Future Work

Further research in this area could be performed to expand upon the conclusions reached. Some possible recommendations for this additional research include:

1. Generation and testing of a full Design of Experiments to examine the effects of all combinations of sinter temperature and hold time.
2. Examine the microstructural and mechanical effects of part orientation during printing.
3. A more thorough analysis on the heat treatment process to determine if a more effective regimen exists for BJP produced parts, such as changes to austenitization temperature and/or hold time as well as the comparison of a double temper to the single temper procedure examined herein.

References

[1] ASM International, *Properties and Selection: Irons, Steels, and High-Performance Alloys*, vol. 1. 1990. [Online]. Available: https://www.asminternational.org/home/-/journal_content/56/10192/06181G/PUBLICATION

[2] G. A. Roberts, R. Kennedy, and G. Krauss, "Tool Steels, 5th Edition." https://books.google.ca/books?hl=en&lr=&id=ScphevR_eP8C&oi=fnd&pg=PA1&dq=tool+steels&ots=PawX1TsBbC&sig=8mDwPHrT1NIcuFvw68uO9SE8Ri8&redir_esc=y#v=onepage&q=tool steels&f=false (accessed Oct. 14, 2020).

[3] ASTM International, "Standard Specification for Tool Steel, Alloy," 2015, doi: 10.1520/A0681-08R15.

[4] ASTM International, "Standard Specification for Tool Steel, Carbon," 2016, doi: 10.1520/A0686-92R16.

[5] ASTM International, "Standard Specification for Tool Steel, High Speed," 2007, Accessed: Oct. 15, 2020. [Online]. Available: https://compass.astm.org/download/A600.9112.pdf

[6] ASM International, *Metallography and Microstructures*, vol. 9. 2004. [Online]. Available: http://www.worldcat.org/oclc/42469467

[7] M. N. Mohammed, M. Z. Omar, J. Syarif, Z. Sajuri, M. S. Salleh, and K. S. Alhawari, "Microstructural evolution during DPRM process of semisolid ledeburitic D2 tool steel," *Sci. World J.*, vol. 2013, pp. 1–7, 2013, doi: 10.1155/2013/828926.

[8] K. Inaekyan, V. Paserin, I. Bailon-poujol, and V. Brailovski, "Binder-jetting additive manufacturing with water atomized iron powders," in *AMPM2016 Conf. Addit.Manuf., Boston, USA*, 2016, pp. 4–6. Accessed: May 14, 2019. [Online]. Available: http://qmp-powders.com/wp-content/uploads/2016-Boston-AMPM2016-Additive-manufacturing-with-water-atomized-powders2.pdf

[9] A. Mostafaei *et al.*, “Binder jet 3D printing—Process parameters, materials, properties, modeling, and challenges,” *Prog. Mater. Sci.*, p. 100707, Jun. 2020, doi: 10.1016/j.pmatsci.2020.100707.

[10] A. J. Pinkerton and L. Li, “Direct additive laser manufacturing using gas- and water-atomised H13 tool steel powders,” *Int. J. Adv. Manuf. Technol.*, vol. 25, no. 5–6, pp. 471–479, Mar. 2005, doi: 10.1007/s00170-003-1844-2.

[11] Y. Zhou, S. C. Siw, M. Orange, C. Schade, and C. I. Garcia, “Sintering behavior of components produced by additive manufacturing using gas versus water atomized 420 stainless steel powders,” in *Materials Science and Technology Conference and Exhibition 2014, MS and T 2014*, 2014, vol. 3, pp. 1993–2002. Accessed: Oct. 27, 2020. [Online]. Available: https://www.researchgate.net/publication/285527214_Sintering_behavior_of_components_produced_by_additive_manufacturing_using_gas_versus_water_atomized_420_stainless_steel_powders

[12] C. T. Schade, T. F. Murphy, C. Walton, and Hoeganaes, “Development of Atomized Powders for Additive Manufacturing,” 2014. Accessed: May 01, 2019. [Online]. Available: https://www.semanticscholar.org/paper/DEVELOPMENT-OF-ATOMIZED-POWDERS-FOR-ADDITIVE-Schade-Murphy/164c56f1e3a3e525162cc28a65d975e2dd39e357

[13] R. Li, Y. Shi, Z. Wang, L. Wang, J. Liu, and W. Jiang, “Densification behavior of gas and water atomized 316L stainless steel powder during selective laser melting,” *Appl. Surf. Sci.*, vol. 256, no. 13, pp. 4350–4356, 2010, doi: 10.1016/j.apsusc.2010.02.030.

[14] M. Ziaee and N. B. Crane, “Binder jetting: A review of process, materials, and methods,” *Additive Manufacturing*, vol. 28. Elsevier B.V., pp. 781–801, Aug. 01, 2019. doi: 10.1016/j.addma.2019.05.031.

[15] Y. Bai and C. B. Williams, “Binder jetting additive manufacturing with a particle-free metal ink as a binder precursor,” *Mater. Des.*, vol. 147, pp. 146–156, Jun. 2018, doi: 10.1016/j.matdes.2018.03.027.

[16] Y. Bai and C. B. Williams, “Binderless Jetting: Additive Manufacturing of metal parts via jetting nanoparticles.” Accessed: Mar. 29, 2021. [Online]. Available: https://www.desktopmetal.com/products/production/

[17] B. WONG and J. A. PASK, *Models for Kinetics of Solid State Sintering*, vol. 62, no. 3–4. 1979, pp. 138–141. doi: 10.1111/j.1151-2916.1979.tb19039.x.

[18] M. Braginsky, V. Tikare, and E. Olevsky, “Numerical simulation of solid state sintering,” in *International Journal of Solids and Structures*, Jan. 2005, vol. 42, no. 2, pp. 621–636. doi: 10.1016/j.ijsolstr.2004.06.022.

[19] R. M. German, “An Update on the Theory of Supersolidus Liquid Phase Sintering.” Accessed: May 07, 2019. [Online]. Available: https://pdfs.semanticscholar.org/f9a0/05b9a6a88eb008ccf20200979696887328 3f.pdf

[20] ASM International, *Powder Metal Technologies and Applications*, vol. 7. 1998.

[21] R. M. German, “Liquid phase sintering,” 2013. doi: 10.1533/9781845699949.1.110.

[22] R. M. German, P. Suri, and S. J. Park, “Review: Liquid phase sintering,” *J. Mater. Sci.*, vol. 44, no. 1, pp. 1–39, Jan. 2009, doi: 10.1007/s10853-008-3008-0.

[23] O. H. Kwon and G. L. Messing, “A theoretical analysis of solution-precipitation controlled densification during liquid phase sintering,” *Acta Metall. Mater.*, vol. 39, no. 9, pp. 2059–2068, Sep. 1991, doi: 10.1016/0956-7151(91)90176-2.

[24] W. A. Kaysser and G. Petzow, “Present State of Liquid Phase Sintering,” *http://dx.doi.org/10.1179/pom.1985.28.3.145*, vol. 28, no. 3, pp. 145–150, Jan. 2013, doi: 10.1179/POM.1985.28.3.145.

[25] R. M. German, “Supersolidus liquid-phase sintering of prealloyed powders,” *Metall. Mater. Trans. A Phys. Metall. Mater. Sci.*, vol. 28, no. 7, pp. 1553–1567, 1997, doi: 10.1007/s11661-997-0217-0.

[26] A. Mostafaei, E. L. Stevens, E. T. Hughes, S. D. Biery, C. Hilla, and M. Chmielus, "Powder bed binder jet printed alloy 625: Densification, microstructure and mechanical properties," *Mater. Des.*, vol. 108, pp. 126–135, Oct. 2016, doi: 10.1016/j.matdes.2016.06.067.

[27] M. Qian, "Metal Powder for Additive Manufacturing," *JOM*, vol. 67, no. 3, pp. 536–537, Mar. 2015, doi: 10.1007/s11837-015-1321-z.

[28] J. C. Najmon, S. Raeisi, and A. Tovar, "Review of additive manufacturing technologies and applications in the aerospace industry," in *Additive Manufacturing for the Aerospace Industry*, Elsevier Inc., 2019, pp. 7–31. doi: 10.1016/B978-0-12-814062-8.00002-9.

[29] S. M. Gaytan *et al.*, "Fabrication of barium titanate by binder jetting additive manufacturing technology," *Ceram. Int.*, vol. 41, no. 5, pp. 6610–6619, 2015, doi: 10.1016/j.ceramint.2015.01.108.

[30] A. Levy, A. Miriyev, A. Elliott, S. S. Babu, and N. Frage, "Additive manufacturing of complex-shaped graded TiC/steel composites," *Mater. Des.*, vol. 118, pp. 198–203, Mar. 2017, doi: 10.1016/j.matdes.2017.01.024.

[31] Tomas Kellner, "An Epiphany Of Disruption: GE Additive Chief Explains How 3D Printing Will Upend Manufacturing," *GE Reports*, pp. 1–10, 2017, Accessed: Nov. 02, 2020. [Online]. Available: https://www.ge.com/news/reports/epiphany-disruption-ge-additive-chief-explains-3d-printing-will-upend-manufacturing

[32] S. Holland, T. Foster, W. MacNaughtan, and C. Tuck, "Design and characterisation of food grade powders and inks for microstructure control using 3D printing," *J. Food Eng.*, vol. 220, pp. 12–19, Mar. 2018, doi: 10.1016/j.jfoodeng.2017.06.008.

[33] C. Deng, J. Kang, H. Shangguan, Y. Hu, T. Huang, and Z. Liu, "Effects of hollow structures in sand mold manufactured using 3D printing technology," *J. Mater. Process. Technol.*, vol. 255, pp. 516–523, May 2018, doi: 10.1016/j.jmatprotec.2017.12.031.

[34] G. L. Huang, S. G. Zhou, and T. Yuan, “Development of a Wideband and High-Efficiency Waveguide-Based Compact Antenna Radiator With Binder-Jetting Technique,” *IEEE Trans. Components, Packag. Manuf. Technol.*, vol. 7, no. 2, pp. 254–260, Feb. 2017, doi: 10.1109/TCPMT.2016.2646386.

[35] J. Ingaglio, J. Fox, C. J. Naito, and P. Bocchini, “Material characteristics of binder jet 3D printed hydrated CSA cement with the addition of fine aggregates,” *Constr. Build. Mater.*, vol. 206, pp. 494–503, May 2019, doi: 10.1016/j.conbuildmat.2019.02.065.

[36] H. Zeidler, D. Klemm, F. Böttger-Hiller, S. Fritsch, M. J. Le Guen, and S. Singamneni, “3D printing of biodegradable parts using renewable biobased materials,” in *Procedia Manufacturing*, Jan. 2018, vol. 21, pp. 117–124. doi: 10.1016/j.promfg.2018.02.101.

[37] E. Mancuso *et al.*, “Three-dimensional printing of porous load-bearing bioceramic scaffolds,” *Proc. Inst. Mech. Eng. Part H J. Eng. Med.*, vol. 231, no. 6, pp. 575–585, Jun. 2017, doi: 10.1177/0954411916682984.

[38] F. Liravi and M. Vlasea, “Powder bed binder jetting additive manufacturing of silicone structures,” *Addit. Manuf.*, vol. 21, pp. 112–124, May 2018, doi: 10.1016/j.addma.2018.02.017.

[39] D. Vogler, S. D. C. Walsh, E. Dombrovski, and M. A. Perras, “A comparison of tensile failure in 3D-printed and natural sandstone,” *Eng. Geol.*, vol. 226, pp. 221–235, Aug. 2017, doi: 10.1016/j.enggeo.2017.06.011.

[40] M. Naitoh, Y. Kubota, A. Katsumata, C. Ohsaki, and E. Ariji, “Dimensional accuracy of a binder jet model produced from computerized tomography data for dental implants.,” *J. Oral Implantol.*, vol. 32, no. 6, pp. 273–276, 2006, doi: 10.1563/1548-1336(2006)32[273:DAOABJ]2.0.CO;2.

[41] S. Infanger, A. Haemmerli, S. Iliev, A. Baier, E. Stoyanov, and J. Quodbach, "Powder bed 3D-printing of highly loaded drug delivery devices with hydroxypropyl cellulose as solid binder," *Int. J. Pharm.*, vol. 555, pp. 198–206, Jan. 2019, doi: 10.1016/j.ijpharm.2018.11.048.

[42] F. Zhang *et al.*, "3D printing technologies for electrochemical energy storage," *Nano Energy*, vol. 40. Elsevier Ltd, pp. 418–431, Oct. 01, 2017. doi: 10.1016/j.nanoen.2017.08.037.

[43] Desktop Metal, "How metal 3D printing can help tooling manufacturers." https://www.desktopmetal.com/industries/tooling (accessed Aug. 29, 2022).

[44] Desktop Metal, "Learn how auto makers are using metal 3D printing." https://www.desktopmetal.com/industries/automotive (accessed Aug. 29, 2022).

[45] Desktop Metal, "How metal 3D printing is changing consumer goods manufacturing." https://www.desktopmetal.com/industries/consumer (accessed Aug. 29, 2022).

[46] M. Li, W. Du, A. Elwany, Z. Pei, and C. Ma, "Metal binder jetting additive manufacturing: A literature review," *J. Manuf. Sci. Eng. Trans. ASME*, vol. 142, no. 9, 2020, doi: 10.1115/1.4047430.

[47] D. Herzog, V. Seyda, E. Wycisk, and C. Emmelmann, "Additive manufacturing of metals," *Acta Mater.*, 2016, doi: 10.1016/j.actamat.2016.07.019.

[48] D. Bourell *et al.*, "Materials for additive manufacturing," *CIRP Ann. - Manuf. Technol.*, vol. 66, no. 2, pp. 659–681, 2017, doi: 10.1016/j.cirp.2017.05.009.

[49] P. K. Gokuldoss, S. Kolla, and J. Eckert, "Additive manufacturing processes: Selective laser melting, electron beam melting and binder jetting-selection guidelines," *Materials*, vol. 10, no. 6. Multidisciplinary Digital Publishing Institute, p. 12, Jun. 19, 2017. doi: 10.3390/ma10060672.

[50] H. Fayazfar *et al.*, "A critical review of powder-based additive manufacturing of ferrous alloys: Process parameters, microstructure and mechanical properties," *Mater. Des.*, vol. 144, pp. 98–128, Apr. 2018, doi: 10.1016/j.matdes.2018.02.018.

[51] H. Attar *et al.*, “Mechanical behavior of porous commercially pure Ti and Ti-TiB composite materials manufactured by selective laser melting,” *Mater. Sci. Eng. A*, 2015, doi: 10.1016/j.msea.2014.12.036.

[52] I. Gibson, D. W. Rosen, and B. Stucker, *Additive Manufacturing Technologies*. Boston, MA: Springer US, 2010. doi: 10.1007/978-1-4419-1120-9.

[53] S. Das, D. L. Bourell, and S. S. Babu, “Metallic materials for 3D printing,” *MRS Bull.*, vol. 41, no. 10, pp. 729–741, Oct. 2016, doi: 10.1557/mrs.2016.217.

[54] U. Ali *et al.*, “Identification and characterization of spatter particles and their effect on surface roughness, density and mechanical response of 17-4 PH stainless steel laser powder-bed fusion parts,” *Mater. Sci. Eng. A*, vol. 756, pp. 98–107, May 2019, doi: 10.1016/J.MSEA.2019.04.026.

[55] R. Esmaeilizadeh, U. Ali, A. Keshavarzkermani, Y. Mahmoodkhani, E. Marzbanrad, and E. Toyserkani, “On the effect of spatter particles distribution on the quality of Hastelloy X parts made by laser powder-bed fusion additive manufacturing,” *J. Manuf. Process.*, vol. 37, pp. 11–20, Jan. 2019, doi: 10.1016/J.JMAPRO.2018.11.012.

[56] Y. Tang, Y. Zhou, T. Hoff, M. Garon, and Y. F. Zhao, “Elastic modulus of 316 stainless steel lattice structure fabricated via binder jetting process,” *Mater. Sci. Technol. (United Kingdom)*, vol. 32, no. 7, pp. 648–656, 2016, doi: 10.1179/1743284715Y.0000000084.

[57] A. Elliott, S. AlSalihi, A. L. Merriman, and M. M. Basti, “Infiltration of Nanoparticles into Porous Binder Jet Printed Parts,” *Am. J. Eng. Appl. Sci.*, vol. 9, no. 1, pp. 128–133, Mar. 2016, doi: 10.3844/AJEASSP.2016.128.133.

[58] M. Dourandish, D. Godlinski, and A. Simchi, “3D Printing of Biocompatible PM-Materials,” *Mater. Sci. Forum*, vol. 534–536, pp. 453–456, 2007, doi: 10.4028/www.scientific.net/msf.534-536.453.

[59] H. Chen and Y. F. Zhao, “Process parameters optimization for improving surface quality and manufacturing accuracy of binder jetting additive manufacturing process,” *Rapid Prototyp. J.*, vol. 22, no. 3, 2016, doi: 10.1108/RPJ-11-2014-0149.

[60] A. C. Bailey, A. Merriman, A. Elliott, and M. M. Basti, “Preliminary testing of nanoparticle effectiveness in binder jetting applications,” in *Solid Freeform Fabrication 2016: Proceedings of the 27th Annual International Solid Freeform Fabrication Symposium - An Additive Manufacturing Conference, SFF 2016*, 2016, pp. 1069–1077. Accessed: Jun. 14, 2019. [Online]. Available: http://energy.gov/downloads/doe-public-

[61] S. Shrestha and G. Manogharan, “Optimization of Binder Jetting Using Taguchi Method,” *JOM*, vol. 69, no. 3, pp. 491–497, Mar. 2017, doi: 10.1007/s11837-016-2231-4.

[62] D. T. Chou, D. Wells, D. Hong, B. Lee, H. Kuhn, and P. N. Kumta, “Novel processing of iron–manganese alloy-based biomaterials by inkjet 3-D printing,” *Acta Biomater.*, vol. 9, no. 10, pp. 8593–8603, Nov. 2013, doi: 10.1016/J.ACTBIO.2013.04.016.

[63] D. Hong *et al.*, “Binder-jetting 3D printing and alloy development of new biodegradable Fe-Mn-Ca/Mg alloys,” *Acta Biomater.*, vol. 45, pp. 375–386, Nov. 2016.

[64] I. Rishmawi, M. Salarian, and M. Vlasea, “Binder jetting additive manufacturing of water-atomized iron,” in *Solid Freeform Fabrication 2018: Proceedings of the 29th Annual International Solid Freeform Fabrication Symposium - An Additive Manufacturing Conference, SFF 2018*, 2018, pp. 160–170.

[65] I. Rishmawi, M. Salarian, and M. Vlasea, “Tailoring green and sintered density of pure iron parts using binder jetting additive manufacturing,” *Addit. Manuf.*, vol. 24, pp. 508–520, Dec. 2018, doi: 10.1016/J.ADDMA.2018.10.015.

[66] ExOne, “Metal 3D Printing Materials & Binders.” https://www.exone.com/en-US/3d-printing-materials-and-binders/metal-materials-binders (accessed Sep. 06, 2021).

[67] H. Miyanaji, N. Momenzadeh, and L. Yang, “Effect of printing speed on quality of printed parts in Binder Jetting Process,” *Addit. Manuf.*, vol. 20, pp. 1–10, Mar. 2018.

[68] R. Frykholm, Y. Takeda, B. G. Andersson, and R. Carlstrom, “Solid state sintered 3-D printing component by using inkjet (binder) method,” *J. Japan Soc. Powder Powder Metall.*, vol. 63, no. 7, pp. 421–426, 2016, doi: 10.2497/jjspm.63.421.

[69] A. Mostafaei, J. Toman, E. L. Stevens, E. T. Hughes, Y. L. Krimer, and M. Chmielus, “Microstructural evolution and mechanical properties of differently heat-treated binder jet printed samples from gas- and water-atomized alloy 625 powders,” *Acta Mater.*, vol. 124, pp. 280–289, Feb. 2017, doi: 10.1016/j.actamat.2016.11.021.

[70] W. J. Sames, F. A. List, S. Pannala, R. R. Dehoff, and S. S. Babu, “The metallurgy and processing science of metal additive manufacturing,” *Int. Mater. Rev.*, vol. 61, no. 5, pp. 315–360, Jul. 2016, doi: 10.1080/09506608.2015.1116649.

[71] MPIF, *Standard Test Methods for Metal Powders and Powder Metallurgy Products*. 2010.

[72] ASTM International, “Standard Test Methods for Rockwell Hardness of Metallic Materials.” https://compass.astm.org/document/?contentCode=ASTM%7CE0018-22%7Cen-US&proxycl=https%3A%2F%2Fsecure.astm.org&fromLogin=true (accessed Dec. 04, 2022).

[73] ASTM International, “Standard Test Methods of Compression Testing of Metallic Materials at Room Temperature.” https://compass.astm.org/document/?contentCode=ASTM%7CE0009-19%7Cen-US (accessed Dec. 04, 2022).

[74] D. Bombac, M. Fazarinc, A. S. Podder, and G. Kugler, “Study of Carbide Evolution During Thermo-Mechanical Processing of AISI D2 Tool Steel,” *J. Mater. Eng. Perform. 2013*, vol. 22, no. 3, pp. 742–747, Aug. 2013, doi: 10.1007/S11665-012-0340-Y.

[75] T. Vecko Pirtovsek, G. Kugler, P. Fajfar, M. Fazarinc, I. Perus, and M. Tercelj, “Hot Forming of AISI D2 tool steel,” *RMZ - Mater. Geoenvironment*, vol. 54, no. 1, pp. 1–14, 2007, [Online]. Available: http://www.dlib.si/details/URN:NBN:SI:DOC-KEMM201M

[76] M. A. Hamidzadeh, M. Meratian, and M. Mohammadi Zahrani, “A study on the microstructure and mechanical properties of AISI D2 tool steel modified by niobium,” *Mater. Sci. Eng. A*, vol. 556, pp. 758–766, Oct. 2012, doi: 10.1016/j.msea.2012.07.061.

[77] H. G. Nanesa, J. Boulgakoff, and M. Jahazi, “Influence of prior cold deformation on microstructure evolution of AISI D2 tool steel after hardening heat treatment,” *J. Manuf. Process.*, vol. 22, pp. 115–119, Apr. 2016, doi: 10.1016/J.JMAPRO.2016.02.002.

[78] Z. Xu, M. A. Hodgson, K. Chang, G. Chen, X. Yuan, and P. Cao, “Effect of sintering time on the densification, microstructure, weight loss and tensile properties of a powder metallurgical Fe-Mn-Si alloy,” *Metals (Basel).*, vol. 7, no. 3, p. 81, Mar. 2017, doi: 10.3390/met7030081.

[79] S. Y. Kondrat’ev, V. S. Kraposhin, G. P. Anastasiadi, and A. L. Talis, “Experimental observation and crystallographic description of M7C3 carbide transformation in Fe-Cr-Ni-C HP type alloy,” *Acta Mater.*, vol. 100, pp. 275–281, Nov. 2015, doi: 10.1016/j.actamat.2015.08.056.

[80] A. I. Gorunov, “Investigation of M7C3, M23C6 and M3C carbides synthesized on austenitic stainless steel and carbon fibers using laser metal deposition,” *Surf. Coatings Technol.*, vol. 401, Nov. 2020, doi: 10.1016/j.surfcoat.2020.126294.

[81] J. Pacyna, “Dilatometric investigations of phase transformations at heating and cooling of hardened, unalloyed, high-carbon steels,” *J. Achiev. Mater. Manuf. Eng.*, vol. 46, no. 1, pp. 7–17, 2011, Accessed: Aug. 25, 2022. [Online]. Available: http://www.journalamme.org/papers_vol46_1/4611.pdf

[82] M. Vardavoulias, G. Papadimitriou, and D. Pantelis, “Effect of M7C3→M23C6 transformation on fracture behaviour of cast ferritic stainless steels,” *Mater. Sci. Technol. (United Kingdom)*, vol. 9, no. 8, pp. 711–717, 1993, doi: 10.1179/mst.1993.9.8.711.

[83] Y. Li, H. Wei, L. Zan, J. Zhang, H. Zheng, and Y. Yu, “Effect of magnesium on the morphology of carbides and on M7C3→M23C6 carbides transformation in the 21-4N heat-resistant steel,” *Ironmak. Steelmak.*, vol. 47, no. 1, pp. 51–58, Jan. 2020, doi: 10.1080/03019233.2019.1680175.

[84] ASM International, *Heat Treating*, vol. 4. 1991.